Journal of Sea Research 198 (2024) 102484

Contents lists available at ScienceDirect

Journal of Sea Research

journal homepage: www.elsevier.com/locate/seares

Simulation of the upper oceanic response to the super cyclonic storm *Amphan* in the Northern Bay of Bengal

Shaila Akhter [a], Fangli Qiao [b,c,*], K M Azam Chowdhury [d], Xunqiang Yin [b,c], Md Kawser Ahmed [d]

[a] Bangladesh Betar, Ministry of Information and Broadcasting, Government of the People's Republic of Bangladesh, Dhaka 1207, Bangladesh
[b] The First Institute of Oceanography, Ministry of Natural Resources, Qingdao 266061, China
[c] Key Laboratory of Marine Science and Numerical Modeling, Ministry of Natural Resources, Qingdao 266061, China
[d] Department of Oceanography & International Centre for Ocean Governance (ICOG), University of Dhaka, Dhaka 1000, Bangladesh

ARTICLE INFO

Keywords:
ROMS model
Model validation
Tropical cyclone
Upwelling
Northern Bay of Bengal

ABSTRACT

The lack of observational data in the northern part of the Bay of Bengal (BoB) makes it challenging to investigate the upper oceanic responses to tropical cyclones. To overcome this challenge, a high-resolution Regional Ocean Model (ROMS) is set up with horizontal resolution of 0.03° × 0.03° and 50 vertical layers for the northern BoB, with the daily output of the First Institute of Oceanography surface wave-tide-circulation coupled ocean model (FIO-COM) as the boundary condition, and hourly ERA5 data as atmospheric forcings. This regional model is systematically validated and then utilized to reconstruct the upper ocean response due to the super cyclonic storm *Amphan* over the BoB from May 16 to 20, 2020. The upper ocean responses to *Amphan* in the northern BoB is well reconstructed with this regional model. On the right side of the cyclone track, sea surface temperature (SST) cooling (4 °C) and increased sea surface salinity (0.5 psu) are well reproduced. The primary oceanic triggering forces intensified the cyclone through the extraordinarily high SST (>31 °C) and deep isothermal layer depth. Tropical cyclone heat potential was high (over 100Kj cm^{-2}) during the early stages of the cyclone, which aided the transformation of a depression into a super cyclonic storm. Vertical entrainment and horizontal advection had a major influence in the pronounced cooling within the mixed layer.

1. Introduction

Due to its subtropical position and warm pool, the Indian subcontinent is one of the most cyclone-prone parts of the Indian Ocean region (Kumar et al., 2019). Although the Bay of Bengal (BoB) and the Arabian Sea are located on the same latitude, the BoB is much more sensitive for the formation of cyclones (Lin et al., 2009). The adjacent rivers supply the BoB with a significant amount of freshwater, and the extra precipitation over evaporation helps to keep the bay fresh and maintain haline stratification (Shenoi et al., 2002; Rao and Sivakumar, 2003; Girishkumar et al., 2013; Pant et al., 2015), which distinguishes it from the Arabian Sea. This haline stratification retains the shallow mixed layer and warmer SST in this bay, making it a powerhouse for the formation of tropical cyclones (Prakash and Pant, 2017). Tropical cyclones are more likely in this bay in the months preceding the monsoon (May–June) and following the monsoon (October–December) (Gray, 1968; Anonymous, 1979; Obasi, 1997; Li et al., 2013). Tropical cyclones are affected by both the surface and subsurface oceans, depending on how strongly the upper ocean mixes vertically. Through the air-sea flux, the oceans contribute energy for cyclone intensification. As a result, tropical cyclones will be intensified by the favorable air conditions; considerable heat transfer from the oceans is also required (Lin et al., 2009), and even plays dominant role for the intensification. Air-sea interactions are the most important driver in the formation and development of tropical cyclones (Wu et al., 2015; McPhaden et al., 2009a). Therefore, the study of oceanic processes during a super cyclone storm in this bay has been an issue of key interest.

There is lack of observational data in the BoB, particularly in the northern part (Masud-Ul-Alam et al., 2020), which makes it challenging to resolve upper oceanic responses during tropical cyclones. Only few buoys and satellite data are options for this type of study, and data from these sources have uncertainties due to the storm and cloudy condition (Prakash and Pant, 2017). Therefore, to investigate the response of different oceanic parameters due to cyclone and the mechanisms of ocean response during cyclones, a reliable high-resolution ocean model is very important.

* Corresponding author at: The First Institute of Oceanography, Ministry of Natural Resources, Qingdao 266061, China.
E-mail address: qiaofl@fio.org.cn (F. Qiao).

https://doi.org/10.1016/j.seares.2024.102484
Received 20 November 2023; Received in revised form 5 February 2024; Accepted 6 February 2024
Available online 7 February 2024

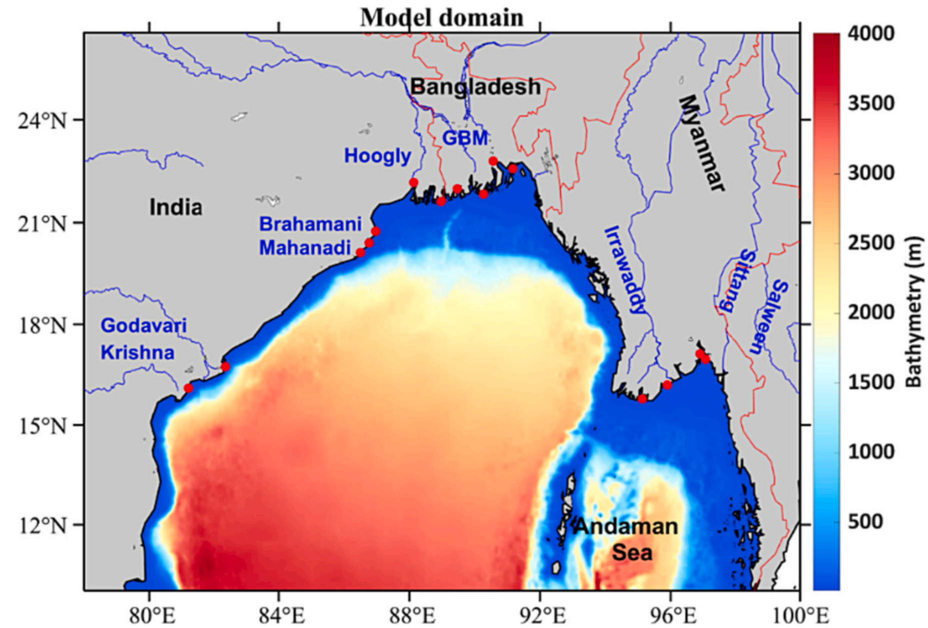

Fig. 1. The topography of the model domain in the northern BoB. GBM stands for Ganges-Brahmaputra-Meghna. The 15 main river mouths along the coast are marked by the red points. The main rivers that were used as freshwater inputs for the regional model are indicated in dark blue. (For interpretation of the references to colour in this figure legend, the reader is referred to the web version of this article.)

In the present study, the Regional Ocean Model (ROMS) was utilized to simulate the tropical cyclone *Amphan*, which formed and traversed in the BoB from 16 May to 21 May 2020. The aim of this research is to estimate the changes in different oceanic processes during this super cyclone and also to explore the mechanisms of the oceanic responses by utilizing the high-resolution regional ocean model.

2. Model set up, data and methods

2.1. Model descriptions

ROMS is an ocean general circulation model, which is three-dimensional, free-surface, non-linear model. ROMS is developed by Rutgers University in the United States and considers the hydrostatic and Boussinesq assumptions to solve the Reynolds averaged Navier-Stokes equations (Danabasoglu et al., 1994; Haidvogel et al., 2000; Shchepetkin and McWilliams, 2005). The S-coordinate is the adopted vertical coordinate system (http://www.myroms. org). ROMS solves the governing equations utilizing boundary-fitted orthogonal, curvilinear coordinates on a staggered Arakawa C grid (Hedstrom, 1997).

This study configured the model for the northern BoB (10°-23°N, 79°-99°E) (Fig. 1) with a high horizontal resolution of (1/30) ° × (1/30) °, and 50 vertical layers. In the zonal direction, it has 602 grid points, and in the meridional direction, 422 grid points. The northern part of the study area is bounded by land and it is considered as closed boundary in the model. The eastern and western boundary of the study area are surrounded by land. Only the southern part of the study area is open to the sea and thus kept to be open boundary. Chapman boundary condition is used for surface elevation (Chapman, 1985). A Flather type radiation condition (Flather, 1987) is used to transport momentum from 2D barotropic energy out of the model domain. For transmitting 3D momentum, the radiation nudging condition is used. The s-coordinate surface and bottom stretching parameters are set to S = 7.0 and B = 0.1, respectively, to improve vertical resolution towards the surface (Song and Haidvogel, 1994). To illustrate vertical mixing, the Mellor-Yamada Level 2.5 Turbulence Closure is utilized (Mellor and Yamada, 1982). The three-dimensional (baroclinic) mode utilizes a 240-s time-step, while the two-dimensional (barotropic) mode employs a 30-s time-step. The water type IA of Jerlov corresponds to penetrative solar radiation (Jerlov, 1968). It may be possible to retain more realistic surface values by relaxing SSS and SST to data (Diansky et al., 2006; Sharma et al., 2010; Nyadjro et al., 2011), however, it compensates for errors in the forcing or model physics artificially. In some parts of the BoB, concluding robust oceanic systems is a tough task (de Boyer Montégut et al., 2004). There is no relaxation to the sea surface temperature and salinity in this paper. High vertical resolution is employed in our configuration between the upper 10 m (6 layers) and 100 m (18 layers), which increases the confidence in the analysis of near-surface processes. These processes include the generation and propagation of surface circulation and freshwater plumes, mixed layer, near-surface saline stratification, barrier layer, and temperature inversion. In the surface and bottom boundary layers, the vertical grid spacing provided higher resolution and prevented artificial diffusion at deep water depths.

2.2. Numerical Ocean model forcings

Surface freshwater flux (Montégut et al., 2007), open boundary condition (Chamarthi et al., 2008), coastal-bay estuarine coupled model (Rao et al., 2007), and volume transfer based on point sources at the coastal boundary are the main modeling parameterizations of the river input. The climatology of monthly discharges of eleven main rivers is employed in this study, and they are mentioned as: 1) Krishna, 2) Godavari, 3) Mahanadi, 4) Brahmani, 5) Hooghly, 6) Ganges, 7) Brahmaputra, 8) Meghna, 9) Irrawaddy, 10) Sittang, and 11) Salween. The Global River Discharge Database (Vörösmarty et al., 1998) along with the Global Runoff Data Centre (GRDC) (Fekete et al., 2000) are the sources of Monthly discharges. Rivers are represented in the model as a collection of point sources that span the coastal boundary, as proposed by Jana et al. (2015). To create a realistic river flow distributary (geographic) in this bay, the discharges of those rivers are separated and arranged in a total of 15 river points (Fig. 1). Each river's discharge is spread evenly along its corresponding location.

The global TPXO8 tidal model generates the amplitude and phase values of eight tidal constituents (M2, S2, N2, K2, K1, O1, P1, Q1) those are used to prescribe tidal forcing along open boundaries (Egbert and Erofeeva, 2002). The Earth Topography 2-minute digital terrain model

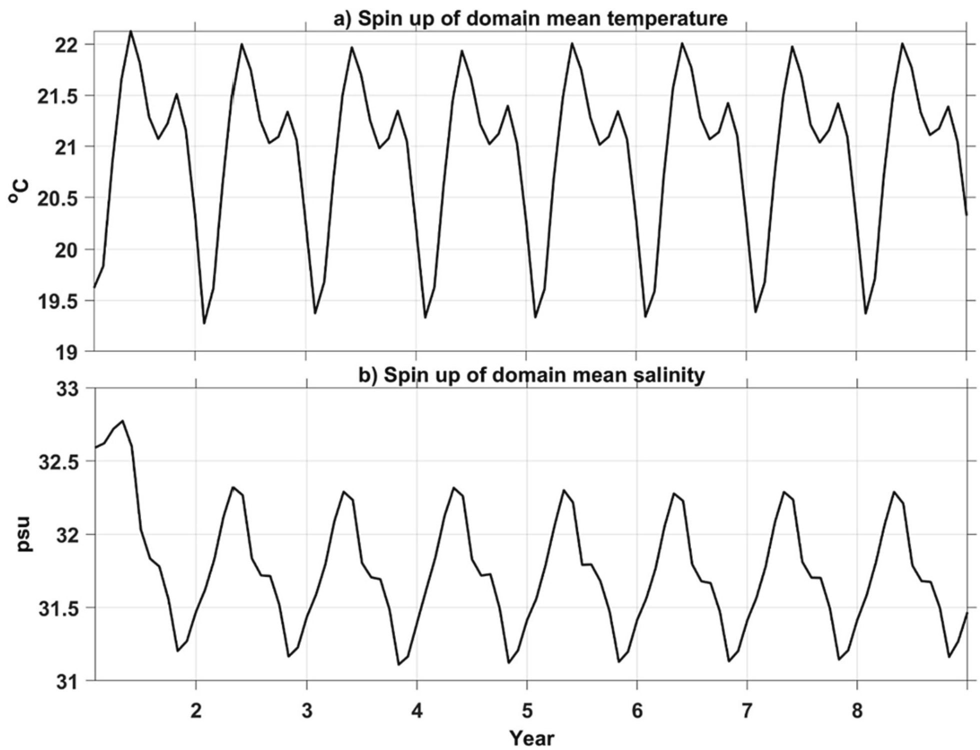

Fig. 2. Spin up of volume averaged temperature (°C) (a), and salinity (psu) (b).

(ETOPO5) output is used to create the bottom topography. At the lateral open boundaries, the model forcing comes from the daily (with a horizontal resolution of 0.1° × 0.1°) temperature, salinity, horizontal sea water velocity and sea surface elevation obtained from the global model, First Institute of Oceanography Coupled Ocean Model (FIO-COM) (Qiao et al., 2018). Starting from a resting state, the model is initialized on 1 January with the daily temperature and salinity specified from the analysis data of FIO-COM, a surface wave-tide-circulation coupled model system. The hourly atmospheric fields used in the model are derived from the European Reanalysis (ERA5), which is the fifth generation of reanalysis published by European Centre for Medium-Range Weather Forecasts (ECMWF) dataset (Berrisford et al., 2009) for the years from 2018 to 2020. The dataset has a horizontal resolution of 0.125° × 0.125°. Notably, ERA5 forcing used in our model includes surface winds, radiations (short wave and long wave), air temperature, air pressure, precipitation rate, and relative humidity. The conventional bulk formula of Fairall et al. (2003) is utilized in the model to calculate the latent and sensible heat fluxes, wind stresses and evaporation. To get a stable spin up 'initial condition', we have simulated the model initially with ERA5 hourly atmospheric forcing for 8 cycles (Fig. 2) for the year 2018 repeatedly. After spin up processes utilizing initial condition, the model is simulated for the years from 2018 to 2020 with boundary forcing from FIO-COM and atmospheric forcing from ERA5, which is considered as the baseline simulation or control run. Hence, baseline simulation is utilized in this study for both validation of the model and further analysis.

2.3. Data sources

2.3.1. Sea surface temperature (SST)

The Optimum Interpolation Sea Surface Temperature (OISST, version 5.0), from remote sensing system (RSS) (www.remss.com), was combined with microwave (MW) and infrared (IR) data. Therefore, MW_IR is the abbreviation for this combination. TMI, AMSR-E, AMSR-2, WindSat, and GMI are among the microwave sensors; MODIS-Terra, MODIS-Aqua, and VIIRS-NPP are among the infrared sensors. Daily is the temporal resolution, while 9 km, or roughly 1/12°, is the horizontal resolution.

2.3.2. Sea surface salinity

This study utilizes the Soil Moisture Active Passive (SMAP) 8-Day running mean gridded sea surface salinity product (version 4.0, level 3). This product with a horizontal resolution of 70 km is derived from the fourth release of operationally developed authenticated standard projected sea surface salinity data of the NASA SMAP observatory. Interpolating the source data generated a spatial resolution of 1/4°(http://www.remss.com/missions/smap).

2.3.3. Temperature and salinity non-gridded (profile) data

Data of temperature and salinity collected by Argo profiling floats (Argo 2000) in the northern BoB were collected through the Global Ocean Data Assimilation Experiment (GODAE) project (http://www.argo.ucsd.edu). Temperature and salinity profile data from a single Argo float with ID2902230 is utilized for 12th and 22th May 2020 to check the effect of cyclone *Amphan*.

Observational data from RAMA mooring buoy, located in the northern BoB at (12°N, 90°E) provides the information on the changes in different atmospheric and oceanic parameters during cyclone *Amphan* (McPhaden et al., 2009b). The data are downloaded for the month of May 2020.

2.3.4. Temperature and salinity gridded data

This study utilizes the EN4 series ocean objective analysis tool (EN4), a new version (version 4) from the UK Met Office Hadley Centre, for the years from 2018 to 2020 (Good et al., 2013). Notably, the name EN comes from two European Union projects: ENACT (Enhanced Ocean Data Assimilation and Climate Prediction; http://www.ecmwf.int/research/EU_projects/ENACT/index.html) and ENSEMBLES (http://ensembles-eu.metoffice.com/index.html) (Ingleby and Huddleston, 2007). The temperature data in this EN4 data version have been adjusted with the Expendable Bathythermograph (XBT) utilizing the Gouretski and Reseghetti technique (Gouretski and Reseghetti, 2010).

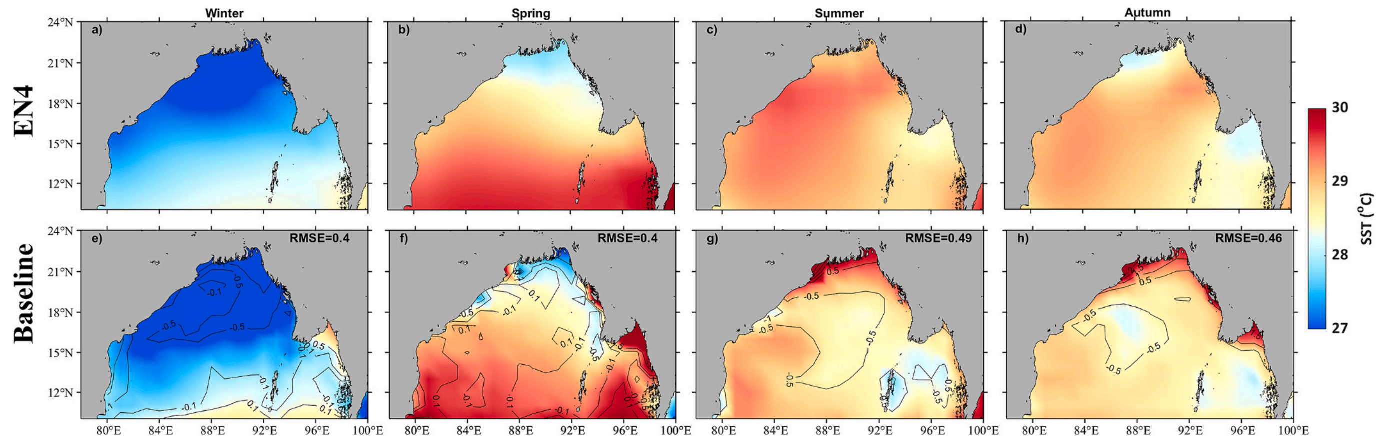

Fig. 3. Comparison of SST (°C) for winter (a, e), spring (b, f), summer (c, g), and autumn (d, h) between EN4 (first row) and baseline simulation (second row), respectively. Contours in the second row indicates the difference of the baseline simulation and EN4.

Monthly temperature and salinity data with a horizontal resolution of 1° by 1° and a vertical resolution of 42 levels from sea surface (5 m) to 5500 m are utilized. In order to make a comparison with EN4 data, the ROMS output with the starting depth of 5 m is also taken into account.

3. Methods

Four seasons are taken into consideration in this study to describe the seasonal fluctuations of different parameters: winter (November–February), spring (March–May), summer (June–August), and autumn (September–October) in accordance with Thadathil et al. (2007) and Narvekar and Kumar (2014). The spatio-temporal variation of mixed layer depth (MLD) has been calculated from EN4 datasets to validate the regional model output. During the cyclone days, temperature and salinity data from RAMA mooring buoy is used to calculate the daily variation of different oceanic parameters including MLD, isothermal layer depth (ILD) (a layer of consistent temperature), ocean heat content and tropical cyclone heat potential (TCHP) and then compared with the daily output of regional model. Additionally, the ROMS model and Argo floats before and after cyclones are also used to calculate these features.

3.1. ILD and MLD calculation

If the temperature from surface to subsurface drop by 0.8 °C, then it is considered as ILD in the current study (Wyrtki et al., 1971; Masson et al., 2002; Rao and Sivakumar, 2003; Thadathil et al., 2007; Shee et al., 2019). The density in water column is used to calculate the MLD from model, EN4 and Argo data. MLD is defined based on depth, where density is equal to the surface density plus the density increment brought on by the 0.8 temperature drop. (Eq. 1) (Kara et al., 2000; de Boyer Montégut et al., 2004; Thadathil et al., 2007; Kumari et al., 2018; He et al., 2020; Chowdhury et al., 2021). The density increment is calculated as follows:

$$\Delta\rho = \rho_t(T + dT, S, P_0) - \rho_t\,(T, S, P_0) \quad (1)$$

Here, T (°C) and S (psu) represent the surface temperature and salinity, respectively; the difference in density between the surface and the MLD is denoted by $\Delta\rho$; ρ_t is the potential density (kg m^{-3}) calculated from the temperature, salinity and reference pressure; and dT is 0.8 °C.

3.2. TCHP and ocean heat content calculation

Tropical cyclones forms in the oceanic regions where SST >26 °C. Therefore, TCHP is marked as the accumulated temperature increment above 26 °C in the water column from sea surface to the depth of the 26 °C isotherm (D26) (Goni et al., 2009):

$$\mathrm{TCHP} = \rho\,\mathrm{Cp}\int_0^{D26}[\mathrm{T(Z)} - 26]\,\mathrm{dz} \quad (2)$$

In this work, the ocean heat content is calculated from the surface to the 23 °C isotherm, which is thought to be the general depth to which the seasonal effect in this bay endures. Therefore, the Ocean heat content is:

$$\text{Ocean heat content} = \rho\,\mathrm{Cp}\int_0^{D23}[\mathrm{T(Z)}]\,\mathrm{dz} \quad (3)$$

The temperature (°C) of each layer of thickness “dz” is represented by T(z) in eqs. (2) and (3), whereas the density of seawater, ρ, is a function of depth, and C_p (3989.2 J kg^{-1} °C) is the specific heat capacity of seawater.

3.3. Ekman pumping velocity

ERA5 provides the wind fields that are higher than 10 m above the ocean surface. These data are used to estimate the wind fields around the cyclone track and the Ekman pumping velocity is calculated as follows:

$$\text{Ekman pumping velocity} = \frac{1}{\rho f}(\nabla \times \tau) \quad (4)$$

Here, density of sea water is denoted by ρ, wind stress is marked as τ, and f defines the Coriolis parameter.

3.4. Mixed layer heat budget analysis

Eq. (5) can be used to characterize the mixed layer heat budget at each grid point in the bay, and in the present study we used this heat budget analysis for a small region following the path of the super cyclonic storm *Amphan*. The “DIAGNOSTICS_TS” option defined by the ROMS model gives us a number of terms that contribute to the temperature change averaged over the MLD (Vialard and Delecluse, 1998; Vialard et al., 2001), stored as daily averages, and grouped as follows:

$$\partial_t T_{ml} = \frac{Q_{net} - Q_{pen}}{\rho\,Cp\,h} - \frac{1}{h}\int_{-h}^{0} u\,\partial_x\,Tdz - \frac{1}{h}\int_{-h}^{0} v\,\partial_y\,Tdz - \frac{1}{h}\int_{-h}^{0} D_l\,(T) + H(W_{23} + \partial_t h)\frac{T_{h+5} - T_h}{h} + \frac{1}{h}K_z\partial_z T + \text{remainder} \qquad (5)\ (a) = \quad (5)$$

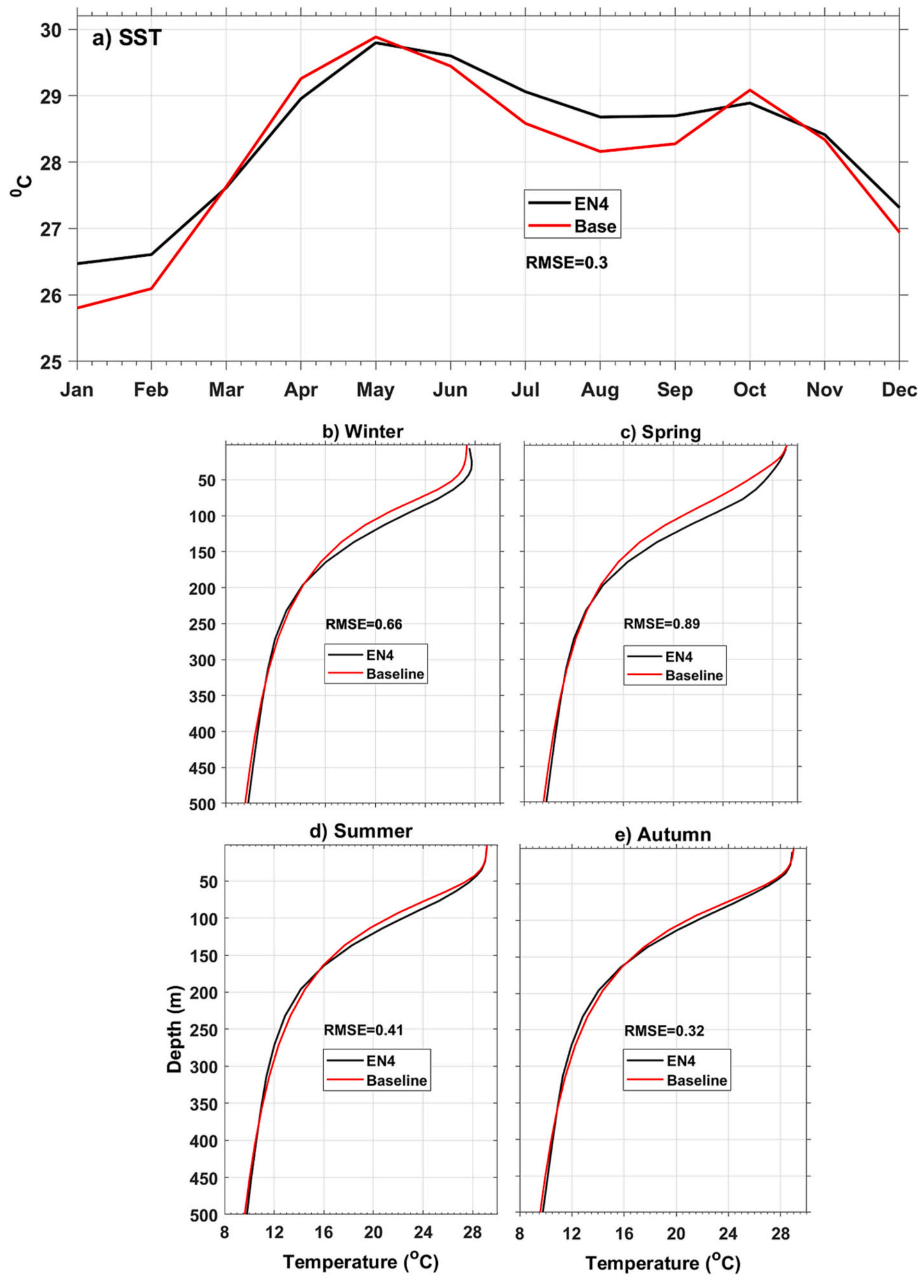

Fig. 4. Monthly variations in basin averaged SST (°C) of EN4 and the baseline simulation (a). Area averaged vertical temperature (°C) profiles during winter (b), spring (c), summer (d), and autumn (e) of EN4 and baseline simulation are compared.

There are eight terms in the balance of this equation. The mixed layer temperature change is described by a variety of terms in the mixed layer heat budget analysis, which aids in the explanation of the upwelling and cooling processes that occur during cyclones (Prakash and Pant, 2017). Here, the term (a) is the temperature tendency of the area-averaged mixed layer; (b) is the mixed layer heat flux; along zonal directions the horizontal advection term of temperature is expressed as term (c), while term (d) is for the meridional directions; term (e) is for lateral processes; (f) term expresses the vertical advection; (g) represents the vertical diffusion; and (h) is the last term representing remainder term. The detail explanation of all these terms in eq. (5) can be found in Chowdhury et al. (2022).

3.5. Root Mean Square Error (RMSE)

RMSE is used to compare an estimated amount with the corresponding observed value. The more accurate a prediction or prognosis, the lower the RMSE value. RMSE is described as:

$$\mathrm{RMSE} = \sqrt{\frac{\sum_{I=1}^{N} (X_{I} - \dot{X}_{I})^2}{N}} \quad (7)$$

In the above equation, I is individual non-missing data points, N is number of non-missing data points, X_I is time series of actual observations, and $\dot{X}_I$ is estimated time series.

4. Model validation

Since the northern BoB is located in the subtropical region, incoming solar radiation has significant contribution in shaping the thermohaline structure of this bay. However, the northmost part of the bay and Andaman Sea are regions of limited in-situ data, mostly devoid of

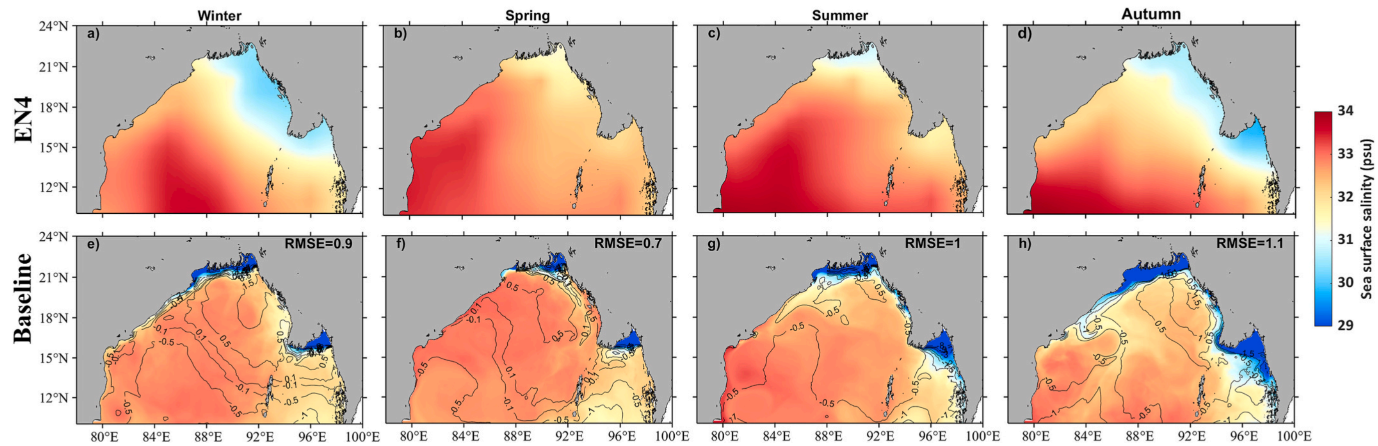

Fig. 5. Comparison of sea surface salinity (psu) for winter (a, e), spring (b, f), summer (c, g), and autumn (d, h) between EN4 (first row) and baseline simulation (second row), respectively. Contours in the second row indicates the difference of baseline simulation and EN4.

temperature and salinity data (Akhil et al., 2014; Masud-Ul-Alam et al., 2020). The datasets that can be used to verify the model performance are quite limited in this area, as there are few Argo floats and nearly no mooring buoys. This study compares the seasonal variation of the temperature, salinity and MLD from the model baseline simulation to the EN4 data.

4.1. Temperature

In the northern BoB, seasonal SST varies strongly and significantly with peaks in spring and autumn. The geographical location of this bay along with the air-sea interactions and presence of summertime huge river discharge as well as rainfall might control the seasonal pattern of SST (Pant et al., 2015; Akhter et al., 2021). Fig. 3 displays the spatial distribution of seasonal SST from EN4 data and model baseline simulation. From EN4 climatology, it is obvious that monthly variation in basin averaged SST in the northern BoB has strong seasonal variation with two peaks during spring and autumn (Figs. 3a-d). SST is low in winter, rises in early spring, and peaks in late spring. The seasonal cycle of SST remains high in summer and again getting a peak in autumn (Figs. 3 and 4a). This basin averaged seasonal SST pattern in the baseline simulation has RMSE of 0.3 °C. Baseline simulation also follows the similar seasonal spatial pattern, with RMSE varying from 0.4 to 0.49 °C (Figs. 3e-h). In winter, the simulated SST is slightly lower than EN4 data at the northern coast of the bay; in other seasons, it is marginally higher. The northern coast is mostly impacted by the freshwater from rivers, and this freshwater driven stratification should be responsible for this bias. However, in this bay, inaccuracy of <1.0 °C in simulated SST is conceivable (Behara and Vinayachandran, 2016; Jana et al., 2018).

Seasonal variation of area averaged vertical profiles from EN4 and baseline simulation is displayed in Fig. 4. The mixed layer detected from observation is also nicely reconstructed by the model. Baseline simulation has followed the observation in capturing the seasonal variation of vertical temperature structure with RMSE varying from 0.36 to 0.87 °C (Figs. 4b-e). Previously it was also found that reconstructing the thermocline in this basin is a challenge and prior reports also indicated that the temperature in thermocline had an RMSE about 1.0 to 2.3 °C (Jana et al., 2015; Chakraborty and Gangopadhyay, 2016).

4.2. Salinity

The spatial distribution of sea surface salinity from EN4 data reveals that the northern tip of the BoB has relatively fresher water than any other region (Figs. 5a-d). There is an increasing tendency in the sea surface salinity from north to south throughout the year. However, the observed sea surface salinity exhibits a significant seasonal variance. The northeastern part of the bay is the only region with low sea surface salinity (<32 psu) in the spring (Fig. 5b). During the summer monsoon period, the northern part of the bay receives excess freshwater discharges, which progressively moves south (Fig. 5c). Some of monsoonal freshwater is even maintained until the winter with a slight temporal lag. However, in spring these freshwater retreats and confined to the far north (Figs. 5a-b). Similar seasonal pattern of sea surface salinity is also presented by Jana et al. (2015).

The spatial pattern of seasonal sea surface salinity depicted by EN4 data is well reproduced by the baseline simulation (Figs. 5e-h). The model can precisely capture the initiation and progression of the monsoonal freshwater flow along the eastern and western coasts (Figs. 5g-h). The model accurately captures the exceptional freshness found along the GBM River system, the major source of freshwater, during the summer and autumn seasons. The model results also adequately depict the freshwater intake from the Irrawaddy River surrounding the Andaman Sea. On the other hand, the simulated sea surface salinity is somewhat larger in offshore of the bay, with RMSE from 0.7 to 1.1 psu around the year and a bigger RMSE (~1.1 psu) in the autumn (Figs. 5e-h). As this area often experiences substantial rainfall, the salty biasness along the northeastern portion of the bay may be the result of an undervaluation of precipitation forced into the model from ERA5 data (Sengupta et al., 2006; Akhil et al., 2014). Basin averaged sea surface salinity shows a similar monthly variation pattern in both the EN4 and baseline simulation with RMSE 0.15 psu (Fig. 6a). The water column of the domain averaged seasonal salinity is in good accordance with EN4 data with a RMSE ranging from 0.12 to 0.16 psu (Figs. 6b-e). Remarkably, salinity bias is mostly present from the surface down to a depth of 100 m in all water column. However, in this region of enormous freshwater sources, modeling of more accurate salinity is still difficult (Vinayachandran et al., 2002; Sengupta et al., 2006; Akhil et al., 2014). In the northern BoB, Masud-Ul-Alam et al. (2022) compare the model and satellite sea surface salinity with the in-situ observations and reported less consistency between them. Scientific community is still working on the improvement for better sea surface salinity simulation.

4.3. MLD

The mixed layer is crucial to the processes of air-sea interaction between the ocean underneath and the atmosphere above, and exchanges mass, momentum and energy between these two layers. The upper ocean thermohaline structure is also controlled by this layer because of its existing location (de Boyer Montégut et al., 2004; Mignot et al., 2007; Francis et al., 2013). This section compares the seasonal variation of basin-averaged MLD from model baseline simulation with EN4 data (Fig. 7). The procedure outlined in section 2.4 is used to calculate both

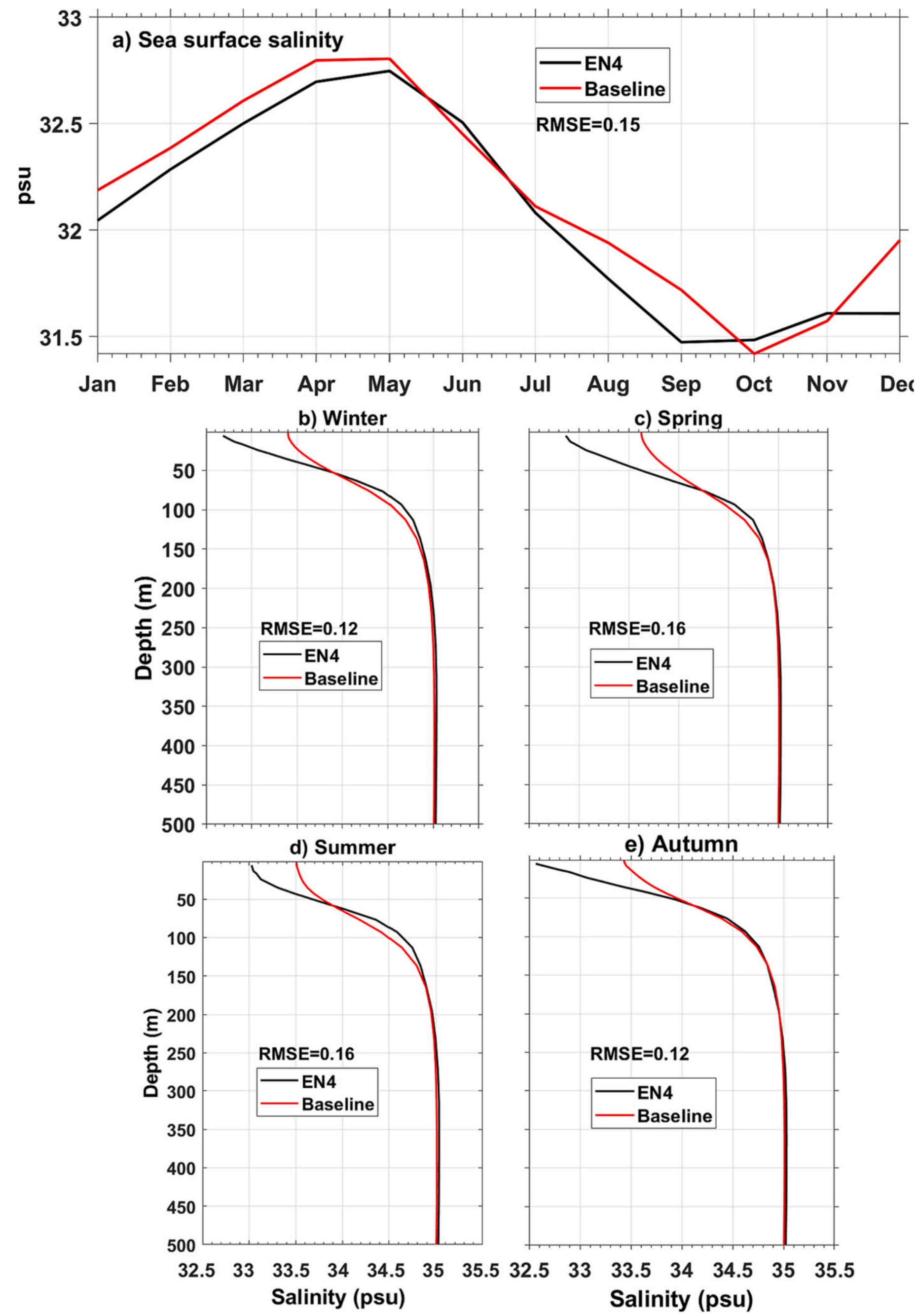

Fig. 6. Monthly variations in basin averaged sea surface salinity (psu) of EN4 and baseline simulation (a). Area averaged vertical salinity (psu) profiles during winter (b), spring (c), summer (d), and autumn (e) of EN4 and model simulation.

observation and model simulated MLD. MLD shows semi-annual variability in this bay, deeper during monsoonal period and shallower between the transition of monsoons (Jana et al., 2015). In the northern BoB, MLD is the lowest in the spring and autumn, somewhat higher in the winter, and the highest in the summer. This seasonal variation of MLD is agreed by the model simulation against the observation (Figs. 7). All the seasonal aspects of MLD are also effectively regenerated in the northern BoB.

In the northern BoB, the spatio-temporal variation of MLD is well generated by the model baseline simulation with RMSE ~7.5 to 10.3 m (Fig. 8). In the northern BoB, MLD remains shallow all the year round (<30 m) having some seasonal variations (Thadathil et al., 2007; Narvekar and Kumar, 2014), which is well captured by the model. The advancement of freshwater plume from the northern coastline to offshore during the summer and autumn exactly matches the shallow MLD from observation and model (Fig. 5), which restricts the MLD about 10 m (Fig. 8). The freshwater mediated haline stratification inhibits mixing and retains the MLD shallow in the northern BoB (Fig. 8c). Freshwater mediated shallow MLD during monsoon is also reported previously (Rao and Sivakumar, 2003; Pant et al., 2015; Prakash and Pant, 2017). During spring, incoming solar radiation is high (Shenoi et al., 2002), which eventually aids to keep the high SST during this season leading a near surface thermal stratification. Shallow MLD in the BoB during spring is the consequences of this thermal stratification. During spring and autumn, weak transitional wind unable to break down the stratification and aid to keep the MLD shallow. However, during winter comparatively deeper MLD is aided by the comparatively strong northeasterly wind. Both surface and water column temperature

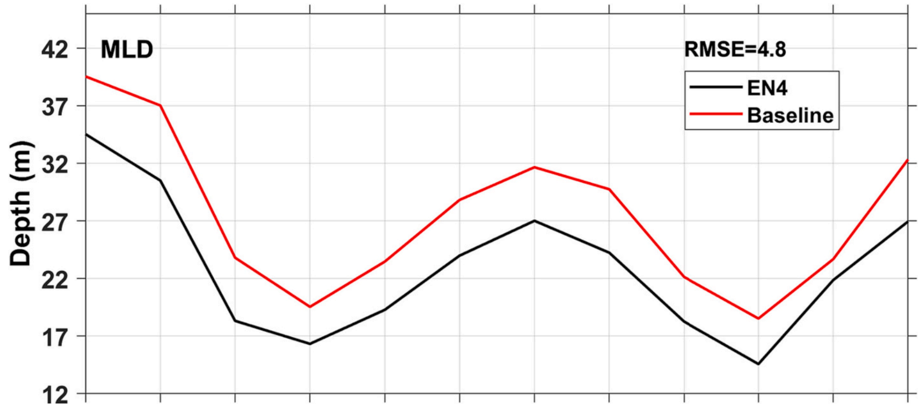

Fig. 7. Monthly variations in basin averaged MLD (m) of EN4 and model simulation.

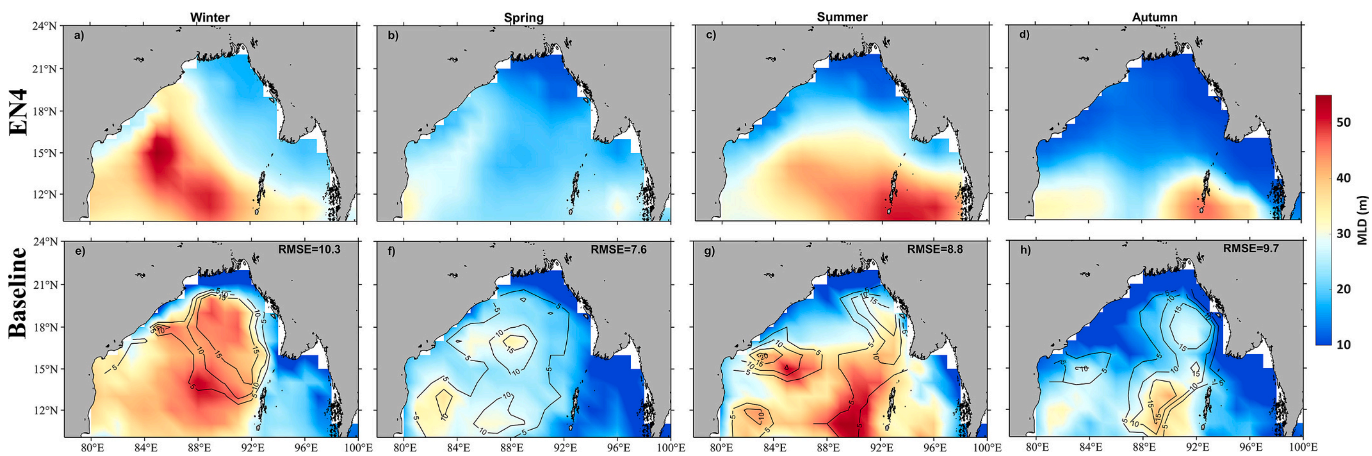

Fig. 8. Comparison of MLD (m) for winter (first column), spring (second column), summer (third column), and autumn (fourth column) between EN4 (first row) and model simulation (second row).

in the northern BoB remain low (Figs. 3a, e), and absence of continental freshwater keep the comparatively deeper MLD, which is nicely reproduced by the model.

5. Ocean model simulation for cyclone *Amphan*

The above validated high-resolution regional model, ROMS is utilized to examine the response of the upper ocean during the super cyclonic storm *Amphan*. Satellite and in situ observations have also been adopted to evaluate pre- and post-cyclone oceanic conditions, as well as to investigate the associated air-sea interaction mechanisms during this cyclone. Using the model simulation, we have analyzed how several oceanic processes contributed to the mixed layer heat budget and SST cooling during cyclone *Amphan*.

5.1. Brief description of cyclone Amphan

Since the 1999 *Odisha* cyclone, *Amphan* was the first super cyclonic storm to hit the BoB with winds above 200 km/h (Ahmed et al., 2021), and it also resulted in the deaths of 72 people in India and 12 in Bangladesh, as well as extensive destruction and damage to public property (Sil et al., 2021; Kumar et al., 2021). In recent years, a westward shift of the formation regions and subsequent tracks for the pre monsoon cyclones has been reported by (Sil et al., 2021). This westward shift allowed Amphan tracks to traverse the warm northward springtime Western Boundary Current (Gangopadhyay et al., 2013) and gather energy from the current and associated warm anti-cyclonic eddies, which ultimately caused the cyclone to intensify. The Indian Meteorology department stated that on May 13, 2020, a low-pressure system over the southeast BoB gave rise to *Amphan* (IMD, 2018). Under the favorable atmospheric conditions, the low-pressure system condensed and deepened into a depression on 16 May 2020, when the SST was warm and vertical wind stress was also low. This depression became a profound depression on the same day but in afternoon. It becomes cyclonic storm in the evening of 16 May by moving to the north and northwestwards, and further intensification turned it into a severe cyclonic storm over the southeastern part of the bay on the next day morning (see the cyclone track in Fig. 9). It went through rapid intensification after that and turned into a very severe cyclonic storm on 17th May afternoon. It developed into a very severe cyclonic storm in the early hours of 18 May 2020, and at noon on that same day, it became a super cyclonic storm. It developed into a very severe cyclonic storm in the early hours of 18 May, and at noon on that same day, it became a super cyclonic storm. The intensity of super cyclonic storm retained for the next 24 h over the west central BoB. During this time, the wind speed was very high (200–250 km/h) and this high wind speed turned the cyclone in category-5 in the Saffir–Simpson scale. During the same time period, the lowest estimated central pressure was 920 hPa. This storm, which made landfall in Bakkhali on 20 May 20, wreaked havoc in West Bengal and Odisha (Fig. 9).

5.2. Simulation of SST and sea surface salinity

SST is one of the key factors in the development and progression of tropical cyclones (Bender et al., 1993; Mahapatra et al., 2007). SST with 26 °C or higher is favorable to form cyclones (Palmen, 1948). High SST

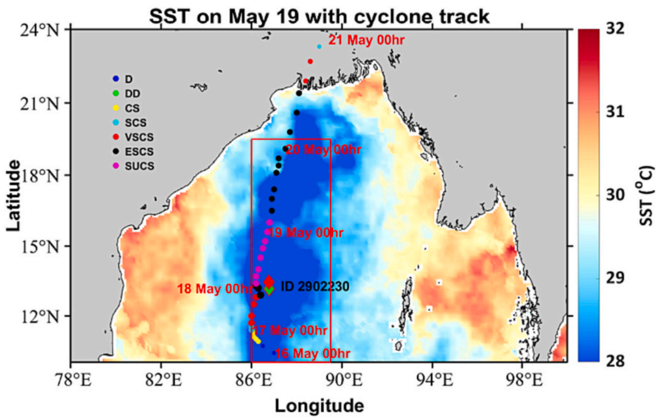

Fig. 9. Distribution of SST (°C) (shading) from MW_IR data sources in the study domain (78° - 100°E, 10° - 24°N) on 19 May (with super cyclonic storm). Using the Saffir-Simpson hurricane wind scale, filled circles with varying colors represent the three-hourly positions of cyclone *Amphan* (IMD, 2018). Here, the terms depression, deep depression, cyclonic storm, severe cyclonic storm, very severe cyclonic storm, very severe cyclonic storm, and super cyclonic storm, respectively, stand for D, DD, CS, SCS, VSCS, ESCS, and SUCS. During Cyclone *Amphan*, the region enclosed by the red rectangular box is taken into account for the estimation of various components of the mixed layer heat budget. Location of Argo float with ID 2902230 before and after cyclone is marked with the diamonds filled with green and red colour, respectively. (For interpretation of the references to colour in this figure legend, the reader is referred to the web version of this article.)

intensifies the storm, while SST cooling reduces the cyclone's intensity (Schade, 2000). During the post cyclone period in the BoB, SST drop of 0.3 °C to 3.0 °C is anticipated, depending on the intensity and trajectory of the cyclones (Rao, 1987; Gopalakrishna et al., 1993; Chinthalu et al., 2001; Subrahmanyam et al., 2005; Sengupta et al., 2006; Kashem et al., 2019).

Fig. 10 shows how SST and sea surface salinity changed during cyclone *Amphan* based on model and satellite observations. For each day between 16 May and 21 Mayof 2020, at 00 UTC, the SST from MW_IR (Figs. 10a-f) and the SST from the model (Figs. 10g-l) are compared. The sea surface salinity from model (Figs. 11g-l) is compared with SMAP (Figs. 10a-f) for corresponding 00 UTC during the cyclone days. Cyclone *Amphan* was formed with very warm SST approximately 30–31 °C covering the northern BoB (Figs. 10a and g). High SST on the eve of cyclone *Amphan* was also reported by Bhowmick et al. (2020). One of the favorable elements for the formation or strengthening of tropical cyclones during the pre- and post-monsoon in the BoB is the higher SST within the 28–30 °C range (McPhaden et al., 2009a). On the very beginning day of cyclone *Amphan* of 16 May, when depression started at the southeast part of the bay cooling observed both from the observation and model (Figs. 10a, g). On the next day cyclone rapidly intensified into a very severe cyclonic storm and the SST decreased >1.0 °C (Figs. 10b, h). Cyclone *Amphan* intensified into a very severe cyclonic storm, and when the SST dropped by >2.0 °C, the cooling patch continued to enlarge (Figs. 10c, i). On 19 May, cyclone *Amphan* intensified extremely followed by SST reduction of >3.5 °C. Cyclone reached in the northern part of the bay and the cooling extended from south to north with the highest cooling patch reaching 4.0 °C (Figs. 10d and j). Highest cooling of 4.0 °C due to cyclone *Amphan* also has been reported (Bhowmick et al., 2020). The cooling also observed on 21 May, when already the landfall occurs. The cooling tendency persisted for a couple of days after *Amphan* landed, according to both the model and satellite data. In accordance with reports that the biggest SST drops are observed in the Northern Hemisphere to the right of the tropical cyclone's track (Black and Dickey, 2008), and in the Southern Hemisphere to the left of the

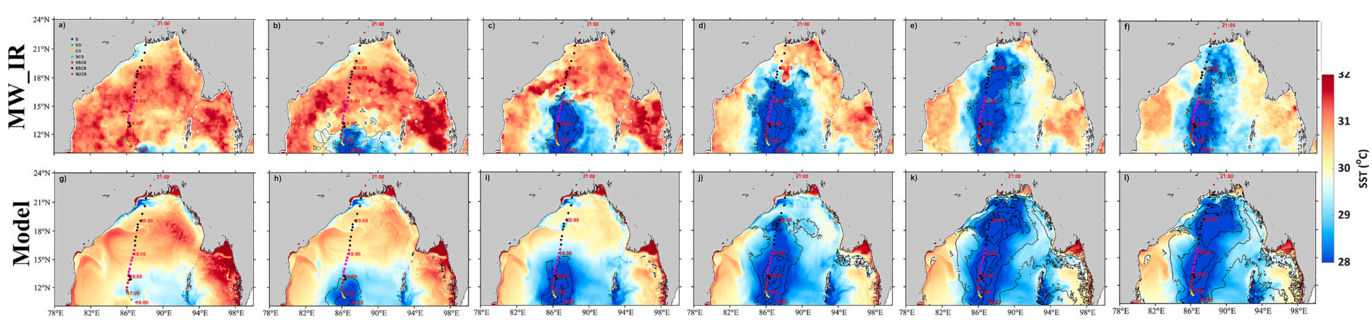

Fig. 10. SST (°C) distribution over the cyclone days (16 to 21 May of 2020) from MW_IR (1st row) and model (2nd row), together with the contours of differences (during cyclone, 17 to 21 May minus starting day of cyclone, 16 October). Along the cyclone track, red-colored numbers represent the date of cyclone at 00 ISC hour. The meanings of D, DD, CS, SCS, VSCS, ESCS, and SuCS in this context are identical to those in Fig. 9. (For interpretation of the references to colour in this figure legend, the reader is referred to the web version of this article.)

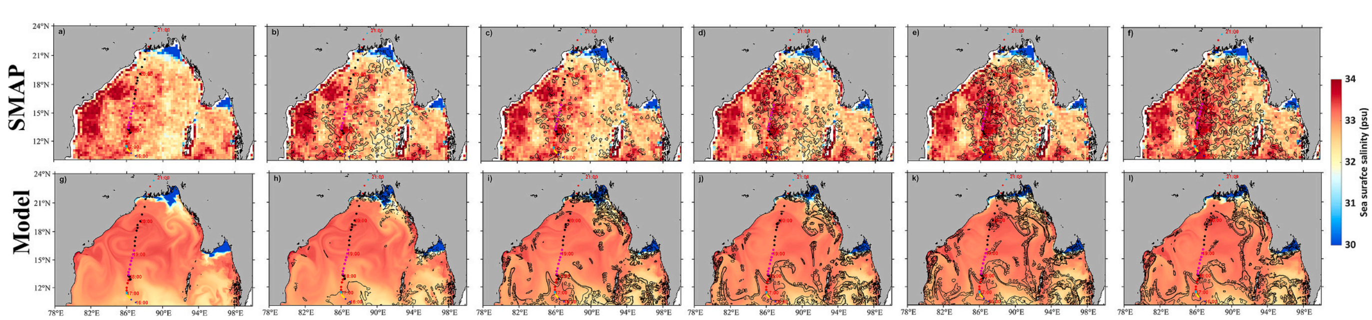

Fig. 11. Sea surface salinity distribution over the cyclone days (16 to 21 May of 2020) from SMAP (1st row) and model (2nd row), together with the contours of differences (during cyclone, 17 to 21 May minus starting day of cyclone, 16 October). Along the cyclone track, the red-colored numbers represent the date of cyclone at 00 ISC hour. The meanings of D, DD, CS, SCS, VSCS, ESCS, and SuCS in this context are identical to those in Fig. 9. (For interpretation of the references to colour in this figure legend, the reader is referred to the web version of this article.)

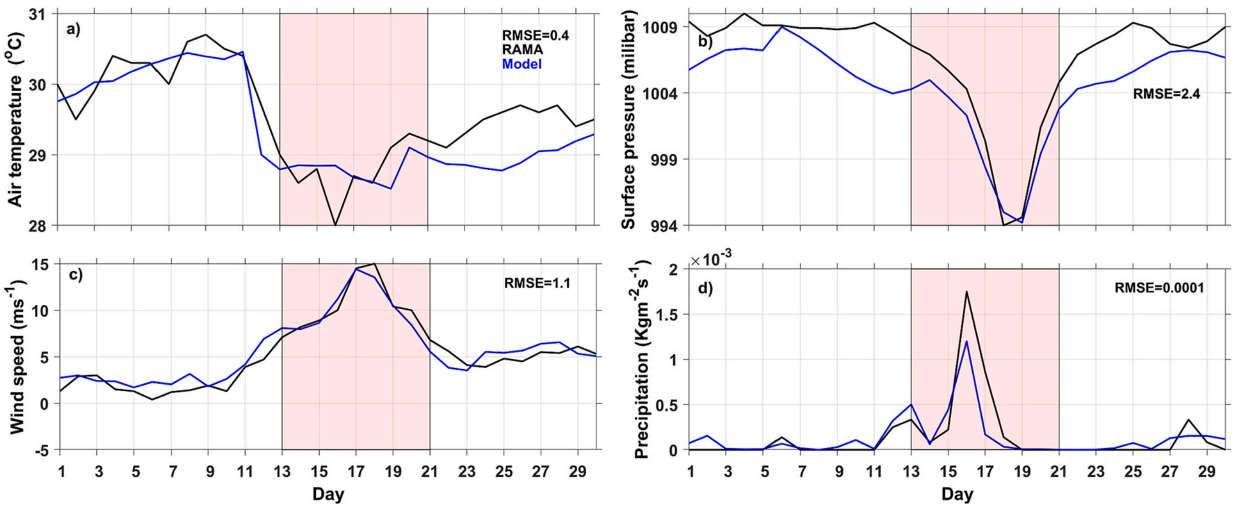

Fig. 12. Daily time series of air temperature (°C) (a), surface pressure (hPa) (b), wind speed (ms^{-1}) (c), and precipitation (Kgm^{-2} s^{-1}) (d) from RAMA observation and ERA5 datasets used as model forcing at position (90°E, 12°N) for the month of May 2020. The light red shaded area indicates the cyclone days. (For interpretation of the references to colour in this figure legend, the reader is referred to the web version of this article.)

track (Berg, 2002), the *Amphan*-caused SST cooling pattern is clearly visible to the right of the track. The regional model output has nicely reproduced the cooling during cyclone *Amphan*, with the shift in SST pattern being extremely similar to satellite data.

In the BoB, a tropical cyclone increases the sea surface salinity while decreasing the SST (McPhaden et al., 2009a; Maneesha et al., 2012; Vinayachandran et al., 2013). Strong cyclonic mixing and interaction of the lower salinity surface water and the saltier subsurface water are expected to rise the sea surface salinity (Sengupta et al., 2006). During cyclone *Amphan*, the sea surface salinity from regional model is in good agreement with SMAP dataset. Sea surface salinity on the first day of Cyclone *Amphan* was around 32 psu north of latitude 11°N (Fig. 11g). Both the model and the observation show that sea surface salinity increases along the cyclone track (Figs. 11a-f and 11g-l).'The most plausible causes of this rise are the turbulent mixing in the overlying mixed layer and entrainment of underneath high saline waters into the mixed layer (McPhaden et al., 2009a). During super cyclonic storm, the increase of sea surface salinity extends from south to north, when the cooling also covers huge area of the bay. On the left side of the cyclone track, sea surface salinity increased mostly in the vicinity of the track; on the right side, an increase in salinity was noted over a considerable region, even surpassing that of the Andaman Sea. Although SST cooling during cyclone *Amphan* was observed about −4.0 °C from both the model and observation, the highest rise in sea surface salinity was 0.5 psu.

5.3. Response of the upper oceans to cyclone Amphan

5.3.1. Temporal variation in atmospheric and oceanic parameters at RAMA (90°E, 12°N)

Figs. 12 and 13 show the time evolution of significant atmospheric and oceanic variables based on RAMA observational data and model simulation. The northern BoB has experienced typical pre-monsoonal conditions prior to the formation of the cyclone *Amphan*. In this region, air temperature has two peaks in the year round having the highest peak during pre-monsoon and before cyclone, this feature was present in this bay (Fig. 12a). Before the cyclone, the sea level pressure was about 1008 hPa, and a weak transitional wind blew over the bay at a speed of 3–4 ms^{-1} (Figs. 12b, c). Precipitation is very unusual in the pre-monsoon period that this feature was also present in this bay before the cyclonic storm (Fig. 12d). The input of these atmospheric parameters to the regional model shows small deviation with low RMSE against the RAMA observational data as revealed from Fig. 12.

Just before the cyclone formation, SST was very high with a value of 31.5 °C and sea surface salinity was low (about 33 psu) (Figs. 13a, b). High SST is the characteristic of pre-monsoon period in the northern BoB. Shallow MLD with shallow ILD was retained before cyclone formation (Figs. 13c-d). As SST remains high in this season, oceanic heat content also remains high with uplifted thermocline. These typical oceanic features were persistent in this bay before the cyclone *Amphan* (Figs. 13e-f). Model simulation also followed the observation very nicely.

It is to be noted that the latent and sensible heat flux components of net surface heat flux, as well as their interactions with the atmosphere and ocean, typically aid depressions in developing into cyclones. When the ocean becomes warmer than the atmospheres, it radiates heat and this eventually is absorbed by the atmosphere. When the ocean heats up faster than the atmosphere, it radiates heat, which is eventually absorbed by the atmosphere. The air temperature was <31 °C from 1 to 12 May 2020 (Fig. 12a), although the SST was consistently higher than 31 °C, demonstrating a constant heat input from the ocean to the atmosphere. As a result of the continued absorption of heat by the atmosphere, a low-pressure system emerged over the Southeastern BoB on May 13, 2020 (Fig. 12b). The sea level pressure got the concave shape when the cyclone formed and persisted till intensified into super cyclone on 19 May 2020 and the minimum pressure was observed to be 995 hPa (Fig. 12b). Cyclone effect is well captured by the model with a small error. Huge rainfall occurred before the highest intensification of cyclone and the wind speed become high (about 15 ms^{-1}) (Figs. 12c, d). SST dropped as a result of this increasing surface wind, and the reduction was significant (>3 °C) (Fig. 13a). Cool SST persisted till the end of the month. In contrast to the strong cooling due to cyclone, sea surface salinity increased very low (~ 0.4 psu) (Figs. 13a, b). High wind and related surface wave induced mixing increases the ILD and deepen the MLD (Figs. 13c, d). High wind speed and cool SST also indicates the deepening of thermocline and reduces the oceanic heat content additionally to the heat potential of tropical cyclones (Figs. 13e-g). Model simulated results have captured this post cyclone effect very well and followed the observation with a small deviation.

Time series of water column temperature for the month of May 2020 from the ROMS model are compared at RAMA buoy locations (90°E, 12°N) (Figs. 14a-b), as other RAMA mooring buoy present in the study domain does not have temperature data during this period. The variability in temperature with high-frequency is observed in buoy data, which is also present in the model temperature profiles. Reduction of vertical temperature from 16 May appeared in both RAMA observation

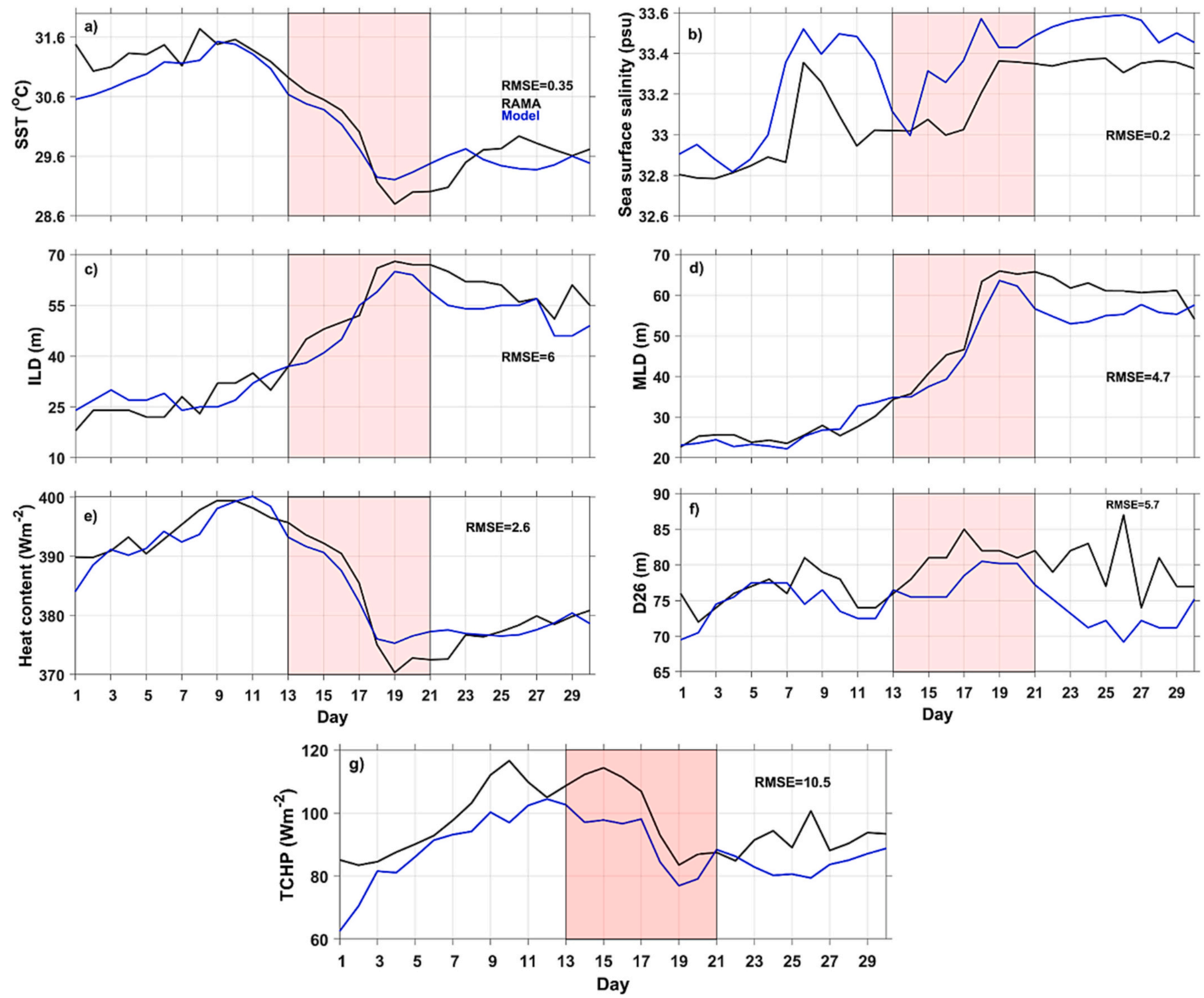

Fig. 13. Time series of daily SST (°C) (a), sea surface salinity (psu) (b), ILD (m) (c), MLD (m) (d), ocean heat content (Wm^{-2}) (e), D26 (m) (f), and TCHP (Wm^{-2}) (g) from RAMA observation and model simulation at position (90°E, 12°N) for the month of May 2020. The light red shaded area indicates the cyclone days. (For interpretation of the references to colour in this figure legend, the reader is referred to the web version of this article.)

and model simulated temperature (Figs. 14a-b). Shallow MLD before the formation of cyclone and the deeper MLD observed in observation after the intensification of cyclone is reconstructed in the model simulation (Fig. 14 b).

5.3.2. Spatial variation of different oceanic characteristics during cyclone

The spatial distributions of the expected change (after cyclone condition minus before cyclone condition of *Amphan*) in SST (°C), sea surface salinity (psu), ILD (m), MLD (m), D26 (m), TCHP (Kj cm^{-2}) and ocean heat content (Kj cm^{-2}) from regional model simulation are presented in Fig. 15. Extensive effect of cyclone *Amphan* on the upper ocean of the study domain is demonstrated by the spatial distribution of anomalies in these parameters. Argo float data from ID2902230 is employed to distinguish the modifications in the abovementioned variables from model. In the pre-cyclone period, Argo float is available on 12 May and in the post-cyclone period, on the 22 May. Therefore, 12 May and 22 May are regarded as the pre-cyclone and post-cyclone periods, respectively, for comparing the model simulated anomalies for different parameters with that of the Argo float data (Table 1).

The spatial distribution of the anomalies in various oceanic parameters from the regional model illustrates the post-cyclone impacts of *Amphan* on the right side of its path. The maximum decrease in SST by approximately 4 °C (Fig. 15a), maximum increase in sea surface salinity by approximately 0.6 psu (Fig. 15b), and the maximum deepening of ILD and MLD by >40 m (Figs. 15c-d) are clearly depicted by the regional model. D26 was shallowed (about 22 m), ocean heat content was reduced (about 70 Kj cm^{-2}), and TCHP was decreased (about 84 Kj cm^{-2}) due to the cyclonic storm *Amphan* (Figs. 15e-g). The strongest wind and related surface wave during cyclonic storm usually generate heavy turbulence, which in turn intensify the vertical mixing (Maneesha et al., 2012). The deeper and colder mixed layer (as seen in Fig. 15d) would result from an inertial oscillation driven on by this strong cyclonic wind force and the turbulent mixing on the right of the cyclone track (Price, 1981).

Amphan reduces SST of the northern BoB from south to north, and the cooling pattern also extended in the Andaman Sea (Fig. 15a), and SST decreases on both sides of the cyclone track. Nevertheless, the SST dropped more on the right side of the cyclone track than that on the left. The Argo float of ID 2902230 located on the right side of the cyclone path showing SST cooling (3.9 °C), which is well reproduced by the

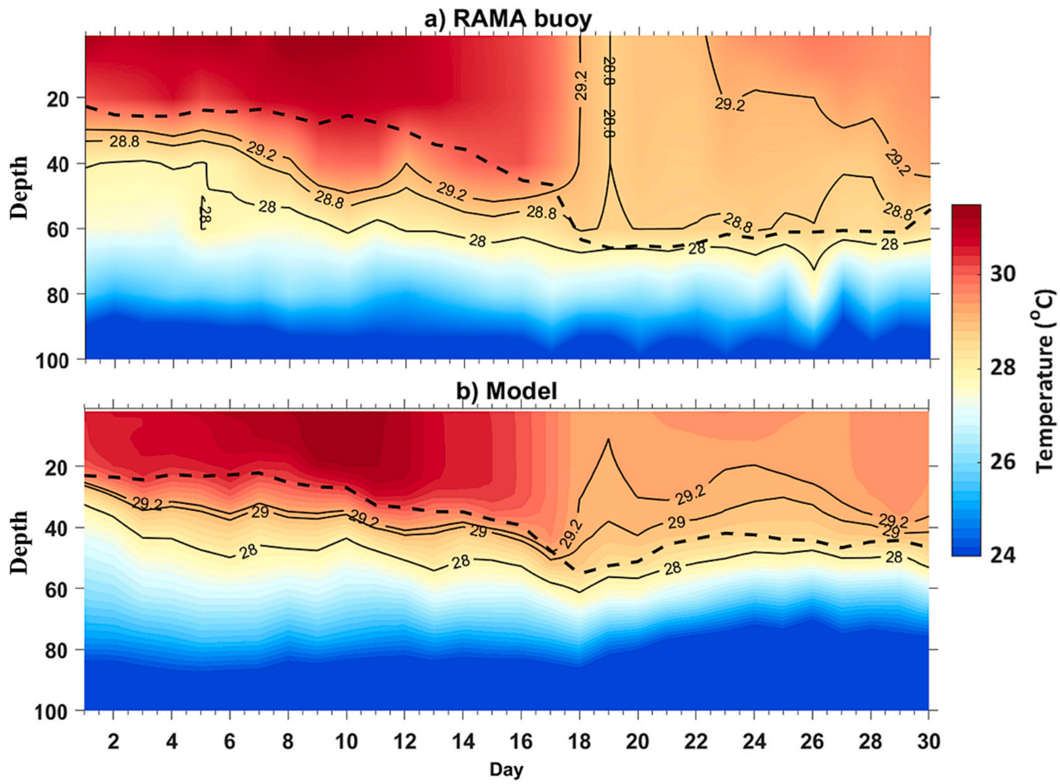

Fig. 14. Time series of water column temperature from RAMA observation (a), and model simulation (b) for the month of May 2020 at location (90°E, 12°N). The black dash line indicates the MLD calculated from the respective data sources.

model (3.8 °C) (Table 1). The increasing area of sea surface salinity due to cyclone *Amphan* did not cover the entire bay. However, area coverage of high saline water was higher on the right than that on the left side of the cyclone track. Both the model and the Argo floats have presented analogous changes in sea surface salinity during cyclone (Fig. 15b; Table 1).

In the post-cyclone period, deeper MLD and ILD are observed on both side of the cyclone track, with the right side being more extended and more intense (Figs. 15 c, d). ILD and MLD have positive anomalies on the right part of the track, which is apparent from both ROMS simulation and Argo observation (Table 1). Shallowing of D26 appeared along the cyclone track from the initial days of the cyclone (Table 1) and shallowing of D26 increases with the increase of the intensity of cyclone. The spatial pattern of heat content anomaly and TCHP due to cyclone have almost alike pattern (Fig. 15f and g). The maximum heat loss during the strong cyclone days occurs within the uppermost 30 m depth (Fig. 15f). The area with the highest SST drop coincided with the maximum heat loss in TCHP along the path of cyclone *Amphan*.

Warmer SST creates a suitable environment for the formation of tropical cyclone because SST modulates the turbulent heat flux (latent and sensible heat fluxes) (Cione, 2015; Sun et al., 2019). Higher SST (>26 °C) is liable for the formation of nearly all tropical cyclones in the Northern Hemisphere. The time series of SST at RAMA mooring position and the spatial variation of SST from model as well as Argo float all show that before generation of cyclone *Amphan*, the SST was about 31.5 °C (Figs. 13a and 15a; Table 1). This extremely high SST is enough to strengthen tropical cyclone (Qiu et al., 2019). However, thermohaline structure of upper ocean also plays key role on the development and strengthening of cyclones. Before the formation of *Amphan,* ILD was deeper (about 25 m), which plays a vital role in intensifying a tropical cyclone (Qiu et al., 2019). Notably, 28 °C of ocean temperature along with 33 Kjcm^{-2} of TCHP can endure a strong storm for a week (Rao, 1987). Cyclone *Amphan* generated with 31.5 °C of SST, about 25 m of ILD and >125 Kjcm^{-2} of TCHP (Table 1). Therefore, the super cyclone *Amphan* was formed and intensified by high SST, high TCHP, and deep ILD; the regional model is able to accurately reproduce the whole processes and their impacts on cyclone *Amphan*.

5.4. *Controlling mechanisms of the upper ocean response during cyclone Amphan*

5.4.1. *Upwelling*

Fig. 16a and d display the structure of water column temperature and salinity from model output in the northern BoB along longitude of 87°E and the latitude ranging from 10 to 20°N on 20 May, one day after the super cyclonic storm on 19 May. Water column structure of temperature and salinity is also provided in the same day from the model output but along the 92°E with the span of same latitude (Figs. 16b-e). Temperature and salinity structures are drawn along the longitude of both 92°E and its parallel along 87°E to observe oceanic change along the cyclone path and a section away from cyclone track. Both temperature and salinity profiles along the 87°E shows the sign of cyclone-induced upwelling. As seen from the observation in MW_IR cooling persisted in the whole bay when the cyclone got the highest intensity, though the enhanced salinity observed from SMAP was a bit weak (Figs. 16c, f). In Figs. 16a-d, the upwelling tendency in the whole bay is also observed; however, a concave up shape form towards surface within 18°N to 19.5°N latitude, where the tropical cyclone *Amphan* induced upwelling contributed 3.5–4.0 °C cooling over the sea surface as well as shoaling is observed along the thermocline (Fig. 16a). A band of high salinity (>34.2 psu) water appears in the upper 60 m, enhancing the sea surface salinity by approximately 0.4 psu in the model outputs within latitudes of 18°N to 19.5°N (Fig. 16d). This pattern resembles to the vertical section of temperature. This elevated salinity is also observed from the SMAP sea surface salinity in the region on the same day of cyclone (Fig. 16f). The significant upwelling signature is also evident when compared to the water column temperature and salinity along the 92°E longitudes (Figs. 6b, e).

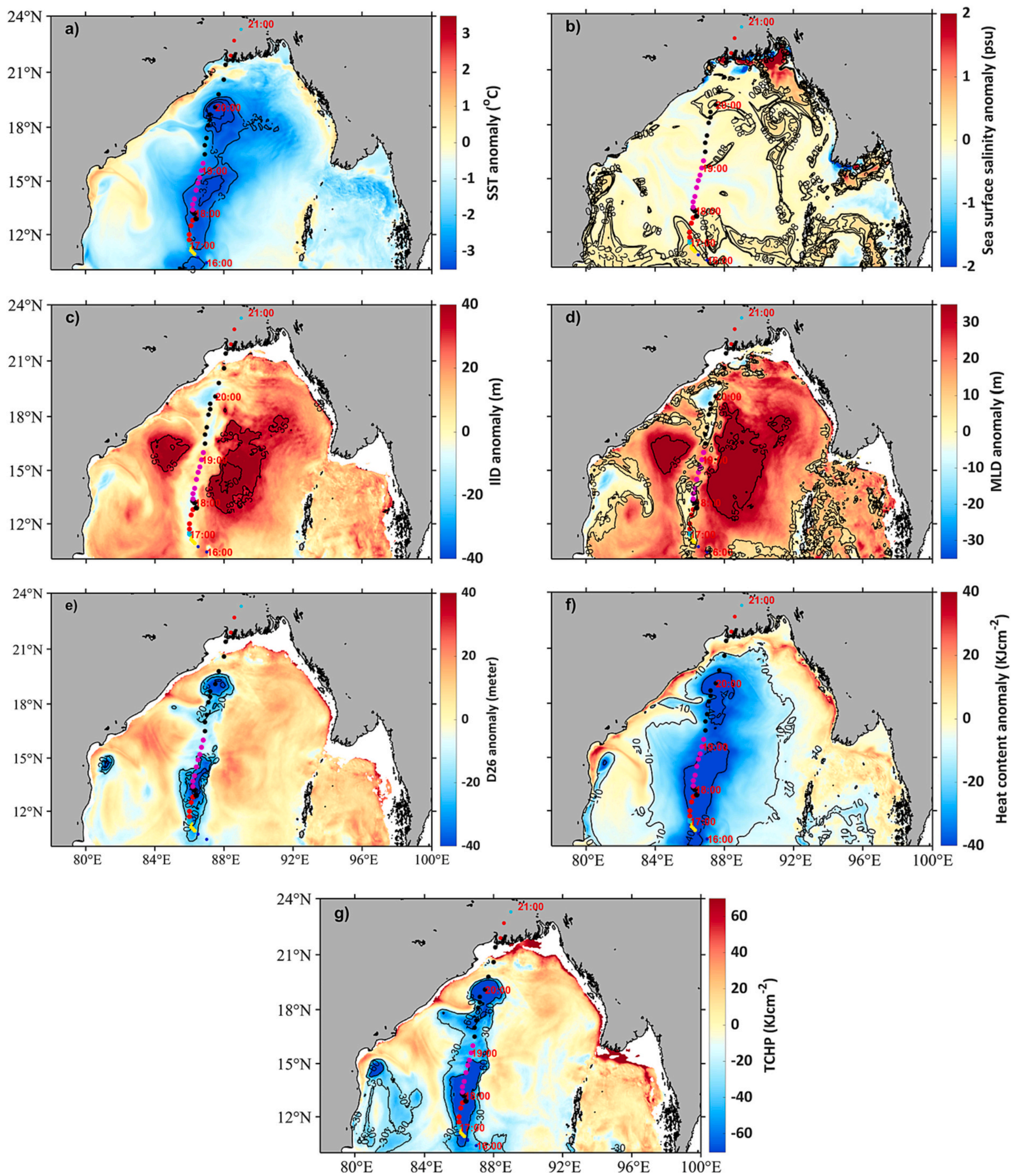

Fig. 15. Estimated differences of SST (°C) (a), sea surface salinity (psu) (b), ILD (m) (c), MLD (m) (d), D26 (m) (e), heat content (Kj cm^{-2}) (f), and TCHP (Kj cm^{-2}) (g) before (12 May) and after (22 May) the cyclone *Amphan* from model outputs.

Wind field has the dominant effect on the upper ocean dynamics, as the wind and related surface wave induced mixing causes the upward Ekman pumping (Stommel, 1958). Upward Ekman pumping causes the upwelling, which uplift the thermocline and eventually cools the SST (Jacob et al., 2000). The Ekman pumping velocity during the days of cyclone *Amphan* estimated from the air-sea flux ERA5, which is adopted in the regional model is displayed in Figs. 17a-d. Ekman pumping velocity is presented here from 17 May. It is observed that a patch of strong Ekman pumping velocity has followed the cyclone path. Strong Ekman pumping velocity along with the strong wind moved with the cyclone track, and the intensity of the velocity and the patch of strong wind became stronger on 19 May, when the cyclone turned into super cyclonic storm. Notably, the upwelling of the thermocline is indicated by a positive Ekman pumping velocity, whereas the downwelling of the thermocline is demonstrated by a negative Ekman pumping velocity (Navaneeth et al., 2019). So, the strong Ekman pumping velocity ($\sim 5 \times 10^{-4}$ ms^{-1}) caused upwelling feature covering huge area on 19 May along the cyclone track (Fig. 17c), which is responsible to cool the SST and enhance salinity in this region as observed in Fig. 17. The modeled vertical velocity during the cyclone days exactly followed the cyclone path similar to Ekman pumping velocity (Figs. 17b and f). Patch of higher vertical velocity observed in the cyclone positions in respective

Table 1
Values of different parameters before and after cyclone from model compared with the Argo floats (ID2902230).

	Before cyclone (86.78° E, 13.16° N)		After cyclone (86.76° E, 13.45° N)		Difference	
	Argo	Model	Argo	Model	Argo	Model
SST (°C)	31.54	31.43	27.64	27.63	−3.9	−3.8
SSS (psu)	32.69	33.05	33.69	33.65	1	0.6
MLD (m)	20.95	22	56.28	63	35.33	41
ILD (m)	25	26	59	66	34	40
D26 (m)	86	66	59	44	−27	−22
HC (Kj cm^{-2})	514.9	506.4	443.6	437.4	−71.4	−69.0
TCHP (Kj cm^{-2})	125.7	138.0	39.3	54.0	−86.3	−84.0

days. This increased vertical velocity emphasizes the upwelling along the cyclone track that is caused by the cyclone. And the highest velocity on 19 May along the cyclone track also indicates the highest upwelling in the super cyclonic storm day (Fig. 17h).

5.4.2. *Intensification of pre-existing cyclonic eddies*

Presence of a considerable number of mesoscale eddies and their dissipation has been reported in BoB (e.g., Sreenivas et al., 2012; Cheng et al., 2013; Sérazin et al., 2015). The East Indian coastal current and local Ekman pumping, in combination with the westward propagating Rossby wave (remote forcing), causes barotropic/baroclinic instability of the mean ocean current, resulting in eddies mostly in the western part of the BoB (Vinayachandran et al., 1999; Somayajulu et al., 2003; Kumar et al., 2004; Chen et al., 2012; Cheng et al., 2018; Gonaduwage et al., 2019; Huang et al., 2019). During the spring and summer, turbulent eddy processes are formed more frequently in this bay than other seasons, with cyclonic eddies (cold core) dominating in the spring and anticyclonic eddies (warm core) dominating in the summer (Cheng et al., 2013; Cui et al., 2016). The upper ocean response to tropical cyclones is influenced by mesoscale eddies, which play an important role in the ocean dynamics (Jacob and Shay, 2003; Mei et al., 2013; Zheng et al., 2010). The upper ocean response due to tropical cyclones appears to be more favorable in cyclonic eddies with a cold core and shallow mixed layer at the center, while tropical cyclone also intensifies cyclonic eddies (Walker et al., 2005; Sun et al., 2019; Vidya and Das, 2017; Chacko, 2017). Eddies and their drivers change the effect of vertical density gradient in the ocean and hence contributing to sea-level anomalies in the BoB (Chen et al., 2012; Sreenivas et al., 2012; Cheng et al., 2013; Cui et al., 2016).

The 6-day average modeled surface current overlaid on the 6-day average sea-level anomaly before and after the cyclone pass as seen in Fig. 18. High sea level and alongshore currents at the southwestern, northern, and eastern boundaries, as well as warm and cold core mesoscale eddies in the bay interior, described the circulation over the bay before the arrival of cyclone *Amphan* (Fig. 18a). The northwestern part of the bay had a pair of warm and cold core eddies before this cyclone. Along the track of cyclone *Amphan*, it had a cold eddy on the left and a warm eddy on the right, with negative (<−0.25 m) and positive (>0.25 m) sea-level anomalies, respectively. The spring time western boundary current (Gangopadhyay et al., 2013) and eddies helped intensify *Amphan* to category 5 (Sil et al., 2021). The super cyclonic storm *Amphan*, caused two significant modifications in the surface circulation (Figs. 18a, b, and c). Firstly, there was a strong northward current on the right side of cyclone *Amphan*'s track, but none on the left side adjacent to the track (Fig. 18c), reflecting the hypothesis

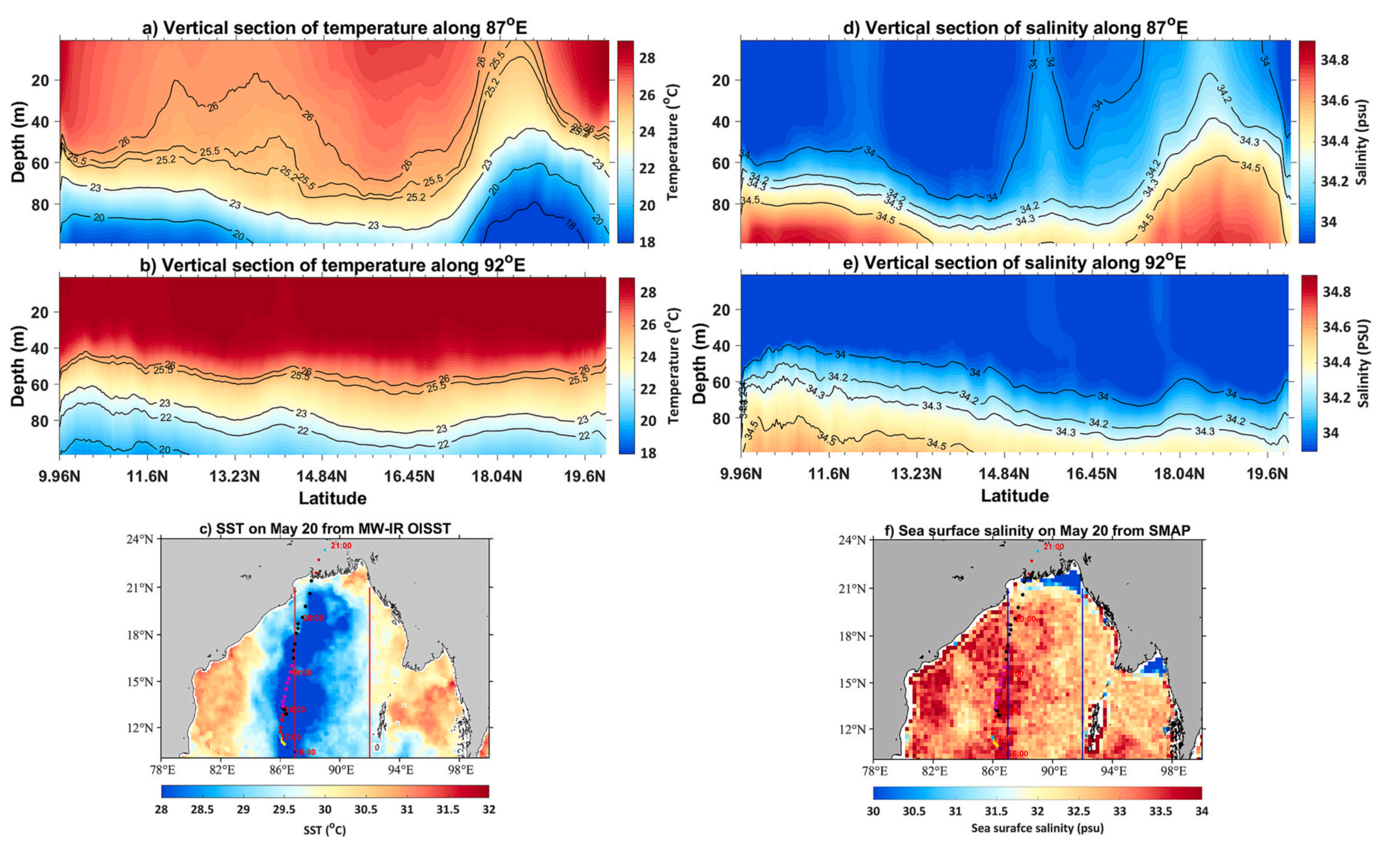

Fig. 16. Vertical sections of temperature (°C) (a, b), and salinity (psu) (d, e), along 87°E and 92°E longitude, respectively from model simulation. SST (°C) from MW_IR (c), and sea surface salinity (psu) from SMAP (f) display the sign of upwelling (more detailed structure of upwelling can be found in Fig. 17). The green and blue lines from south to north in c and f indicates 87°E and 92°E longitude, respectively. (For interpretation of the references to colour in this figure legend, the reader is referred to the web version of this article.)

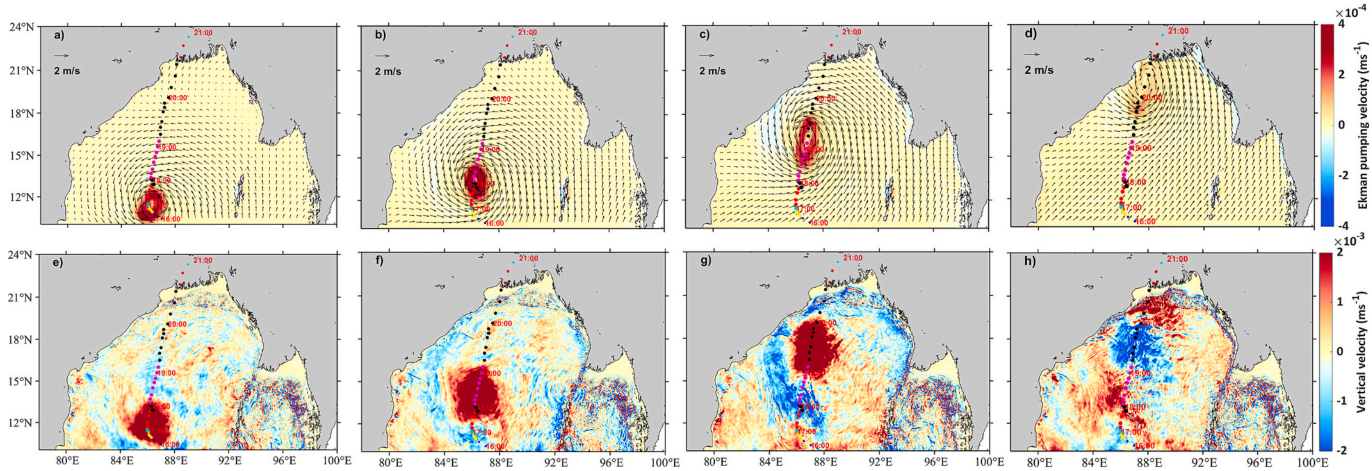

Fig. 17. Ekman pumping velocity (ms^{-1}, shaded) overlaid with the wind vector during the intense cyclone days and the modeled vertical velocity on 17 May (a, e), 18 May (b, f), 19 May (c, g), and 20 May (d, h), respectively. The average vertical velocity of the model is within the top 50 m of the ocean.

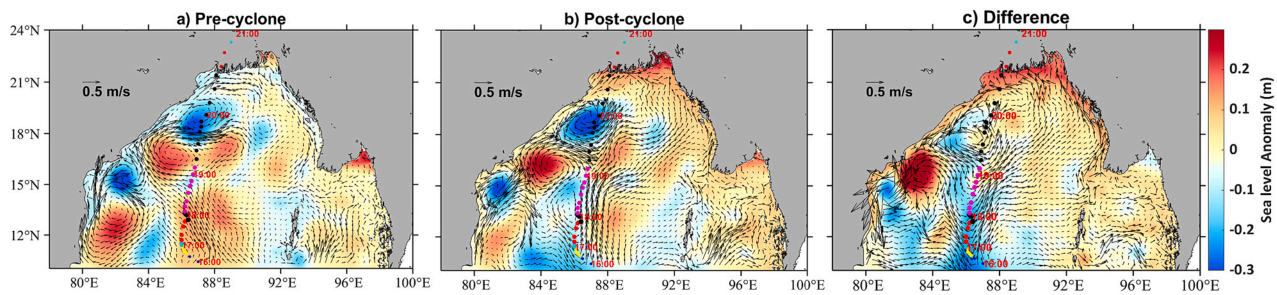

Fig. 18. 6-day averaged sea surface current overlaid on the 6-day averaged sea-level anomaly from model simulation in the study area during pre-cyclone days of 10–15 May 2020 (a), post-cyclone days during 22–27 May 2020 (b), and difference in sea-level anomaly and current between pre- and –post cyclone period (c).

that near-surface velocity in the Northern Hemisphere is always biased rightward (Chang et al., 2016) due to strong wind there (Qiu et al., 2019). Sil et al. (2021) also reported the movement of cyclone *Amphan* close to the positive sea-level anomaly and rightward current biasness. Secondly, while the pre-existing warm eddy was less affected by the tropical cyclone, the pre-existing cold eddy was substantially intensified (Fig. 18b). The intensification of cyclonic eddies causes the reduction of sea-level anomaly after the cyclone passes (Fig. 18c), which could have contributed to the significant SST cooling observed distant from the cyclone track (Fig. 18a). The enhanced alongshore currents on the left side of the track (Fig. 18c) might be associated with the geostrophic flow of the cold eddies (Qiu et al., 2019).

5.4.3. Roles of different oceanic processes

The temporal variation of area-averaged temperature profile during the cyclone days (16 May to 22 May) along with the MLD (black dash line) and D26 (red dash line) are shown in Fig. 19a. The area-average temperature profile is considered for the box in Fig. 9, where the maximum cooling occurs due to the cyclonic upwelling. Initially, when the cyclone was located in the southern part of the bay, temperature was higher and MLD was shallower (~25 m) within the marked box. However, with the arrival of the cyclone, temperature reduced during the intense cyclone days (18 May to 20 May) and the MLD got deeper (~40 m) as well the shallowing of thermocline occurred. Wind field following the cyclone path also became stronger during these days (Figs. 17a-d).

From the model simulated result, a mixed layer heat budget analysis is executed across the boxed region and highlighted in Fig. 9 to assess the relative roles of different oceanic processes in controlling sea surface cooling along the passage of the cyclone *Amphan* (see Fig. 19). A time-series is created by averaging the various elements of the mixed layer heat budget, including temperature tendency, vertical entrainment, horizontal advection, and net heat flux. This time-series is shown in Fig. 19b. Typically, the residual term denotes the unresolved processes, like turbulent mixing and diffusion. Cooling of mixed layer during the cyclone days is evident from the temperature tendency term. The temperature tendency curve shows negative tendency when the cyclone started to intensify. When the cyclone becomes more intensified, rapid increase in negative tendency is observed and the highest negative tendency attained one day after the super cyclonic storm, when it again turned into extremely severe cyclonic storm and very severe cyclonic storm later on. The combined effects of vertical entrainment, horizontal advection, and low net heat flux at the sea surface should be responsible for the cooling of the mixed layer. Within the selected region for mixed layer heat budget analysis, vertical entrainment contributed up to 0.1 $^{\circ}$Cday^{-1}, whereas advection of colder water contributed up to 0.06 $^{\circ}$Cday^{-1} (cooling rate) (Fig. 18b).

The magnitude of negative temperature tendency was a bit lower before 19 May, when vertical entrainment showed positive tendency but other heat budget terms are slightly negative. During 19 May to 20 May, the vertical entrainment term exhibited the negative sign and contributed to the cooling of mixed layer dominantly. During 18 to19 May, the net heat flux also contributed negatively to the temperature tendency. Notably, at the end of 20 May, the horizontal advection term changed its sign and contributed to a slight warming in the mixed layer. The net heat flux and vertical entrainment also contribute to the warm mixed layer during these days. Upwelled cold water advected to this region, followed by warm water from the enhanced net heat flux transited to this region after the passage of cyclone *Amphan*. The mixed layer heat budget analysis reveals that the vertical entrainment and horizontal advection dominantly controlled the cooling phase of the mixed layer during the

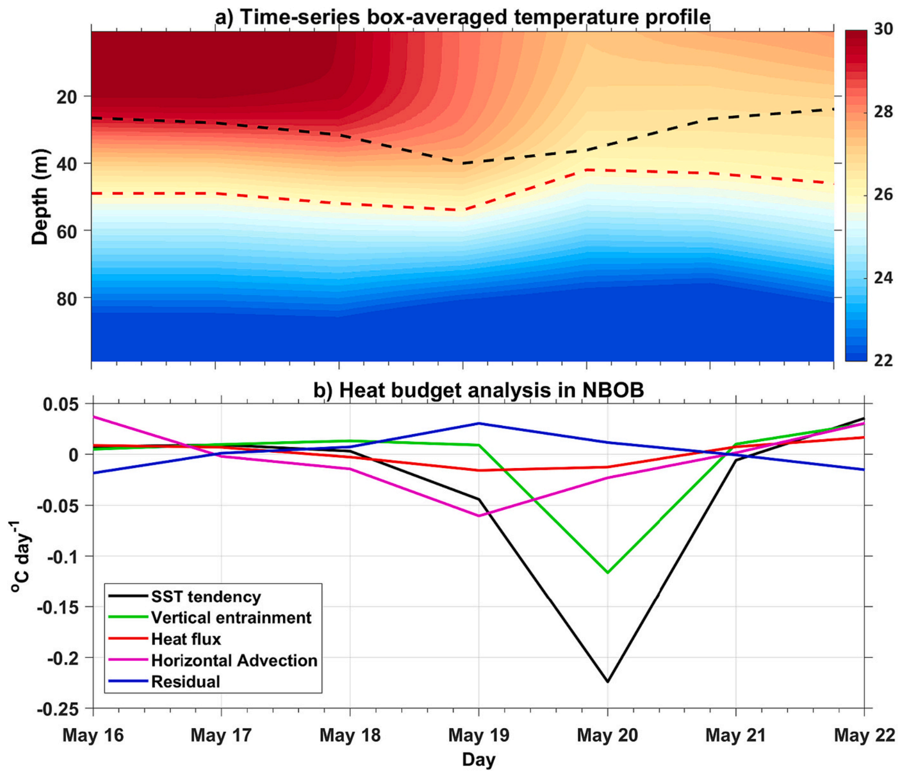

Fig. 19. Time series temperature profile overlaid with MLD (m) (black dash line) and D26 (m) (red dash line) (a), components of mixed layer heat budget (b) of box-averaged (red rectangular box in Fig. 9) model output. (For interpretation of the references to colour in this figure legend, the reader is referred to the web version of this article.)

tropical cyclone *Amphan*. The net heat flux and entrainment clearly govern the temperature tendency of the mixed layer after the passage of *Amphan*.

6. Conclusion

The northern BoB is a unique basin for receiving excessive freshwater from rivers and being proximate to the tropical cyclone formation hub. Furthermore, lack of data availability in this region urges us to set up a high-resolution regional ocean model for present and future studies. The present study focuses on investigating the mechanisms of upper ocean responses to the super cyclone *Amphan* over the BoB from 16 to 20 May 2020 based on a high resolution (horizontal resolution 0.03° x 0.03° with 50 vertical layer) regional ocean model, ROMS, in the area of (10°-23°N, 78°-100°E). This regional model is set up utilizing the daily output from the global operational ocean forecasting system, FIO-COM, as the ocean boundary forcing and hourly ERA5 data as atmospheric forcing. Accordingly, the spatio-temporal variation of temperature, salinity, and MLD are well reproduced by the model in the study domain.

Model and remote sensing data indicate that from 16 to 20 May 2020, there was a substantial decrease of the SST (approximately 4 °C) and an increase in sea surface salinity (~ 0.4 psu) heavily on the right side of the cyclone track. Extremely high SST (>31 °C) and deep ILD were favorable for intensifying the cyclone *Amphan*. At the beginning of cyclone *Amphan*, TCHP was high (>100 Kjcm^{-2}), which further enhanced a depression into a super cyclonic storm. Enhanced positive Ekman pumping in the northern BoB caused upwelling, which uplifted thermoclines and isohalines. Through mixed layer heat budget analysis, the significant role of horizontal advection and vertical entrainment in governing the pronounced cooling of the mixed layer in the north-western BoB between 18 and 20 May 2020 is identified. The upwelled cold water and then advected is mainly responsible for the area-averaged sea surface temperature decrease.

CRediT authorship contribution statement

Shaila Akhter: Writing – original draft, Visualization, Validation, Software, Methodology, Formal analysis, Data curation. **Fangli Qiao:** Writing – review & editing, Supervision, Conceptualization. **K M Azam Chowdhury:** Validation, Methodology, Formal analysis. **Xunqiang Yin:** Formal analysis, Investigation. **Md Kawser Ahmed:** Writing – review & editing, Methodology, Conceptualization.

Declaration of competing interest

The authors declare that they have no known competing financial interests or personal relationships that might have appeared to influence the work reported in this research paper.

Data availability

Data will be made available on request.

Acknowledgments

This research was supported by the National Natural Science Foundation of China under grant 41821004. This research was a contribution to the UN Decade of Ocean Science for Sustainable Development (2021−2030) through both the Decade Collaborative Centre on Ocean-Climate Nexus and Coordination Among Decade Implementing Partners in P. R. China (DCC-OCC) and the approved Programme of the Ocean to climate Seamless Forecasting system (OSF).

References

Ahmed, R., Mohapatra, M., Dwivedi, S., Giri, R.K., 2021. Characteristic features of super cyclone 'AMPHAN'-observed through satellite images. Trop. Cyclone Res. Rev. 10 (1), 16–31. https://doi.org/10.1016/j.tcrr.2021.03.003.

Akhil, V.P., Durand, F., Lengaigne, M., Vialard, J., Keerthi, M.G., Gopalakrishna, V.V., Deltel, C., Papa, F., de Boyer, Montégut C., 2014. A modeling study of the processes of surface salinity seasonal cycle in the Bay of Bengal. J Geophys Res Oceans 119 (6), 3926–3947. https://doi.org/10.1002/2013JC009632.

Akhter, S., Qiao, F., Wu, K., Yin, X., Chowdhury, K.A., Chowdhury, N.U.M.K., 2021. Seasonal and long-term sea-level variations and their forcing factors in the northern Bay of Bengal: a statistical analysis of temperature, salinity, wind stress curl, and regional climate index data. Dyn Atmos Oceans 95, 101239. https://doi.org/10.1016/j.dynatmoce.2021.101239.

Anonymous, 1979. Tracks of Storms and Depressions in the Bay of Bengal and the Arabian Sea 1877–1970. India Meteorological Department, New Delhi.

Behara, A., Vinayachandran, P.N., 2016. An OGCM study of the impact of rain and river water forcing on the Bay of Bengal. J Geophys Res Oceans 121 (4), 2425–2446. https://doi.org/10.1002/2015JC011325.

Bender, M.A., Ginis, I., Kurihara, Y., 1993. Numerical simulations of tropical cyclone-ocean interaction with a high-resolution coupled model. J. Geophys. Res. Atmos. 98 (D12), 23245–23263. https://doi.org/10.1029/93JD02370.

Berg, R., 2002. Tropical cyclone intensity in relation to SST and moisture variability: a global perspective. In: Proceedings of the 25th Conference on Hurricanes and Tropical Meteorology, American Meteorological Society, San Diego, CA, USA, 29 April–3 May 2002.

Berrisford, P., Dee, D.P.K.F., Fielding, K., Fuentes, M., Kallberg, P., Kobayashi, S., Uppala, S., 2009. The ERA-Interim Archive, ERA Report Series, vol. 1. European Centre for Medium-Range Weather Forecasts.

Bhowmick, S.A., Agarwal, N., Sharma, R., Sundar, R., Venkatesan, R., Prasad, C.A., Navaneeth, K.N., 2020. Cyclone Amphan: oceanic conditions pre and post-cyclone using in situ and satellite observations. Curr. Sci. 119, 1510–1516.

Black, W.J., Dickey, T.D., 2008. Observations and analyses of upper ocean responses to tropical storms and hurricanes in the vicinity of Bermuda. J Geophys Res Oceans 113 (C8), C08009. https://doi.org/10.1029/2007JC004358.

Chacko, N., 2017. Chlorophyll bloom in response to tropical cyclone Hudhud in the Bay of Bengal: bio-Argo subsurface observations. Deep Sea Res Part I Oceanogr Res Papers 124, 66–72. https://doi.org/10.1016/j.dsr.2017.04.010.

Chakraborty, A., Gangopadhyay, A., 2016. Development of a high-resolution multiscale modeling and prediction system for Bay of Bengal, part I: climatology-based simulations. Open J Mar Sci 6 (1), 145–176. https://doi.org/10.4236/ojms.2016.61013.

Chamarthi, S., Ram, P.S., Josyula, L., 2008. Effect of river discharge on Bay of Bengal circulation. Mar. Geod. 31 (3), 160–168. https://doi.org/10.1080/01490410802265476.

Chang, K.I., Zhang, C.I., Park, C., Kang, D.J., Ju, S.J., Lee, S.H., Wimbush, M. (Eds.), 2016. Oceanography of the East Sea (Japan Sea). Springer International Publishing, Cham, Switzerland, p. 460.

Chapman, D.C., 1985. Numerical treatment of cross-shelf open boundaries in a barotropic coastal ocean model. J. Phys. Oceanogr. 15 (8), 1060–1075. https://doi.org/10.1175/1520-0485(1985)015%3C1060:NTOCSO%3E2.0.CO;2.

Chen, G., Wang, D., Hou, Y., 2012. The features and interannual variability mechanism of mesoscale eddies in the Bay of Bengal. Cont. Shelf Res. 47, 178–185. https://doi.org/10.1016/j.csr.2012.07.011.

Cheng, X., Xie, S.P., McCreary, J.P., Qi, Y., Du, Y., 2013. Intraseasonal variability of sea surface height in the Bay of Bengal. J Geophys Res Oceans 118, 816–830. https://doi.org/10.1002/jgrc.20075.

Cheng, X., McCreary, J.P., Qiu, B., Qi, Y., Du, Y., Chen, X., 2018. Dynamics of eddy generation in the Central Bay of Bengal. J Geophys Res Oceans 123, 6861–6875. https://doi.org/10.1029/2018JC014100.

Chinthalu, G.R., Seetaramayya, P., Ravichandran, M., Mahajan, P.N., 2001. Response of the Bay of Bengal to Gopalpur and Paradip super cyclones during 15–31 October 1999. Curr. Sci. 81 (3), 283–291.

Chowdhury, K.M.A., Jiang, W.S., Liu, G.M., Ahmed, M.K., Akhter, S., 2021. Dominant physical-biogeochemical drivers for seasonal variations in surface chlorophyll-a and subsurface chlorophyll-a maximum in the Bay of Bengal. Reg. Stud. Mar. Sci. 48, 102022 https://doi.org/10.1016/j.rsma.2021.102022.

Chowdhury, K.M.A., Jiang, W.S., Bian, C.G., Liu, G.M., Ahmed, M.K., Akhter, S., 2022. Contributions of shortwave radiation to the formation of temperature inversions in the Bay of Bengal and eastern equatorial Indian Ocean: a modeling approach. Acta Oceanol Sin 41, 19–37. https://doi.org/10.1007/s13131-022-1998-0.

Cione, J.J., 2015. The relative roles of the ocean and atmosphere as revealed by buoy air–sea observations in hurricanes. Mon. Weather Rev. 143 (3), 904–913. https://doi.org/10.1175/MWR-D-13-00380.1.

Cui, W., Yang, J., Ma, Y., 2016. A statistical analysis of mesoscale eddies in the Bay of Bengal from 22–year altimetry data. Acta Oceanol. Sin. 35, 16–27. https://doi.org/10.1007/s13131-016-0945-3.

Danabasoglu, G., Biringen, S., Streett, C.L., 1994. Application of the spectral multidomain method to the Navier-stokes equations. J. Comput. Phys. 113 (2), 155–164. https://doi.org/10.1006/jcph.1994.1127.

de Boyer Montégut, C., Madec, G., Fischer, A.S., Lazar, A., Iudicone, D., 2004. Mixed layer depth over the global ocean: An examination of profile data and a profile-based climatology. J. Geophys. Res. 109 (C12003) https://doi.org/10.1029/2004JC002378.

Diansky, N.A., Zalesny, V.B., Moshonkin, S.N., Rusakov, A.S., 2006. High resolution modeling of the monsoon circulation in the Indian Ocean. Oceanology 46 (5), 608–628. https://doi.org/10.1134/S000143700605002X.

Egbert, G.D., Erofeeva, S.Y., 2002. Efficient inverse modeling of barotropic ocean tides. J. Atmos. Oceanic Tech. 19 (2), 183–204. https://doi.org/10.1175/1520-0426(2002)019%3C0183:EIMOBO%3E2.0.CO;2.

Fairall, C.W., Bradley, E.F., Hare, J.E., Grachev, A.A., Edson, J.B., 2003. Bulk parameterization of air–sea fluxes: updates and verification for the COARE algorithm. J. Climate 16 (4), 571–591. https://doi.org/10.1175/1520-0442(2003)016%3C0571:BPOASF%3E2.0.CO;2.

Fekete, B.M., Vorosmarty, C.J., Grabs, W., 2000. Global, composite runoff fields based on observed river discharge and simulated water balances. In: Documentation for UNHGRDC Composite Runoff Fields, vol. 1.0. Global Runoff Data Center, Koblenz, Germany.

Flather, R.A., 1987. A tidal model of the Northeast Pacific. Atmosphere-Ocean 25 (1), 22–45. https://doi.org/10.1080/07055900.1987.9649262.

Francis, P.A., Vinayachandran, P.N., Shenoi, S.S.C., 2013. The Indian Ocean forecast system. Curr. Sci. 104 (10), 1354–1368.

Gangopadhyay, A., Bharath Raj, N., Chaudhuri, A., Babu, M.T., Sengupta, D., 2013. On the nature of meandering of the springtime western boundary current in the Bay of Bengal. Geophys. Res. Lett. 40, 1–6. https://doi.org/10.1002/grl.50412.

Girishkumar, M.S., Ravichandran, M., McPhaden, M.J., 2013. Temperature inversions and their influence on the mixed layer heat budget during the winters of 2006-2007 and 2007-2008 in the Bay of Bengal: thermal inversion in the bay of Bengal. J Geophys Res Oceans 118, 2426–2437. https://doi.org/10.1002/jgrc.20192.

Gonaduwage, L.P., Chen, G., McPhaden, M.J., Priyadarshana, T., Huang, K., Wang, D., 2019. Meridional and zonal eddy-induced heat and salt transport in the Bay of Bengal and their seasonal modulation. J Geophys Res Oceans 124 (11), 8079–8101. https://doi.org/10.1029/2019JC015124.

Goni, G., DeMaria, M., Knaff, J., Sampson, C., Ginis, I., Bringas, F., Mavume, A., Lauer, C., Lin, I.I., Ali, M.M., Halliwell, G., 2009. Applications of satellite-derived ocean measurements to tropical cyclone intensity forecasting. Oceanogr 22 (3), 190–197. https://doi.org/10.5670/oceanog.2009.78.

Good, S.A., Martin, M.J., Rayner, N.A., 2013. EN4: quality controlled ocean temperature and salinity profiles and monthly objective analyses with uncertainty estimates. J. Geophys. Res. Oceans 118, 6704–6716. https://doi.org/10.1002/2013JC009067.

Gopalakrishna, V.V., Murty, V.S.N., Sarma, M.S.S., Sastry, J.S., 1993. Thermal response of upper layers of Bay of Bengal to forcing of a severe cyclonic storm: a case study. Indian J Mar Sci 22, 8–11.

Gouretski, V., Reseghetti, F., 2010. On depth and temperature biases in bathythermograph data: development of a new correction scheme based on analysis of a global ocean database. Deep Sea Res Part I Oceanogra Res Pap 57 (6), 812–833. https://doi.org/10.1016/j.dsr.2010.03.011.

Gray, W.M., 1968. Global view of the origin of tropical disturbances and storms. Mon Wea Rev 96, 669–700. https://doi.org/10.1175/1520-0493(1968)096<0669:GVOTOO>2.0.CO;2.

Haidvogel, D.B., Arango, H.G., Hedstrom, K., Beckmann, A., Malanotte-Rizzoli, P., Shchepetkin, A.F., 2000. Model evaluation experiments in the North Atlantic Basin: simulations in nonlinear terrain-following coordinates. Dyn Atmos Oceans 32 (3–4), 239–281. https://doi.org/10.1016/S0377-0265(00)00049-X.

He, S., Peng, Y., Jin, Y., Wan, B., 2020. Research on design and pressure-retaining performance of the pressure-retaining sampler for full-ocean-depth sediment. Int. J. Mater. Prod. Technol. 60 (2–4), 161–179. https://doi.org/10.1504/IJMPT.2020.110116.

Hedstrom, K.S., 1997. SCRUM Manuel, Institute of Marine and Coastal Sciences. RutgersUniversity, USA.

Huang, K., Wang, D., Han, W., Feng, M., Chen, G., Wang, W., Chen, J., Li, J., 2019. Semiannual variability of Middepth zonal currents along 5°N in the eastern Indian Ocean: characteristics and causes. J. Phys. Oceanogr. 49, 2715–2729. https://doi.org/10.1175/JPO-D-19-0089.1.

IMD, 2018. Very Severe Cyclonic Storm "TITLI" over Bay of Bengal (07–13 Oct. 2018) And Very Severe Cyclonic Storm "LUBAN" over Arabian Sea (06–14 October 2018). India Meteorological Department. https://reliefweb.int/sites/reliefweb.int/files/resources/20181016_pr_347.pdf. Accessed 1 September 2021.

Ingleby, B., Huddleston, M., 2007. Quality control of ocean temperature and salinity profiles—historical and real-time data. J. Mar. Syst. 65, 158–175.

Jacob, S.D., Shay, L.K., 2003. The role of oceanic mesoscale features on the tropical cyclone–induced mixed layer response: a case study. J. Phys. Oceanogr. 33 (4), 649–676. https://doi.org/10.1175/1520-0485(2003)33%3C649:TROOMF%3E2.0.CO;2.

Jacob, S.D., Shay, L.K., Mariano, A.J., Black, P.G., 2000. The 3D oceanic mixed layer response to hurricane Gilbert. J Physic Oceanogr 30 (6), 1407–1429. https://doi.org/10.1175/1520-0485(2000)030%3C1407:TOMLRT%3E2.0.CO;2.

Jana, S., Gangopadhyay, A., Chakraborty, A., 2015. Impact of seasonal river input on the Bay of Bengal simulation. Cont. Shelf Res. 104, 45–62. https://doi.org/10.1016/j.csr.2015.05.001.

Jana, S., Gangopadhyay, A., Lermusiaux, P.F., Chakraborty, A., Sil, S., Haley Jr., P.J., 2018. Sensitivity of the Bay of Bengal upper ocean to different winds and river input conditions. J. Mar. Syst. 187, 206–222. https://doi.org/10.1016/j.jmarsys.2018.08.001.

Jerlov, N.G., 1968. Optical Oceanography. In: Elsevier Oceanography Series. Amsterdam, London and New York, vol. 5, p. 194.

Kara, A.B., Rochford, P.A., Hurlburt, H.E., 2000. An optimal definition for ocean mixed layer depth. J Geophys Res Oceans 105 (C7), 16803–16821. https://doi.org/10.1029/2000JC900072.

Kashem, M., Ahmed, M.K., Qiao, F., Akhter, M.A.E., Chowdhury, K.M.A., 2019. The response of the upper ocean to tropical cyclone Viyaru over the Bay of Bengal. Acta Oceanol Sin 38 (1), 61–70. https://doi.org/10.1007/s13131-019-1370-1.

Kumar, S.P., Nuncio, M., Narvekar, J., Kumar, A., Sardesai, D.S., de Souza, S.N., Gauns, M., Ramaiah, N., Madhupratap, M., 2004. Are eddies nature's trigger to enhance biological productivity in the Bay of Bengal? Geophys. Res. Lett. 31 (7), L07309. https://doi.org/10.1029/2003GL019274.

Kumar, P., Kaur, S., Weller, E., Min, S.K., 2019. Influence of natural climate variability on the extreme ocean surface wave heights over the Indian Ocean. J Geophys Res Oceans 124 (8), 6176–6199. https://doi.org/10.1029/2019JC015391.

Kumar, R., Rani, S., Maharana, P., 2021. Assessing the impacts of Amphan cyclone over West Bengal, India: a multi-sensor approach. Environ. Monit. Assess. 193 (5), 1–21. https://doi.org/10.1007/s10661-021-09071-5.

Kumari, A., Kumar, S.P., Chakraborty, A., 2018. Seasonal and interannual variability in the barrier layer of the Bay of Bengal. J Geophys Res Oceans 123 (2), 1001–1015. https://doi.org/10.1002/2017JC013213.

Li, Z., Yu, W., Li, T., Murty, V.S.N., Tangang, F., 2013. Bimodal character of cyclone climatology in Bay of Bengal modulated by monsoon seasonal cycle. J. Climate 26 (3), 1033–1046. https://doi.org/10.1175/JCLI-D-11-00627.1.

Lin, I.I., Chen, C.H., Pun, I.F., Liu, W.T., Wu, C.C., 2009. Warm ocean anomaly, air sea fluxes, and the rapid intensification of tropical cyclone Nargis (2008). Geophys. Res. Lett. 36 (3), L03817. https://doi.org/10.1029/2008GL035815.

Mahapatra, D.K., Rao, A.D., Babu, S.V., Srinivas, C., 2007. Influence of coast line on upper ocean's response to the tropical cyclone. Geophys. Res. Lett. 34 (17), L17603. https://doi.org/10.1029/2007GL030410.

Maneesha, K., Murty, V.S.N., Ravichandran, M., Lee, T., Yu, W., McPhaden, M.J., 2012. Upper Ocean variability in the Bay of Bengal during the tropical cyclones Nargis and Laila. Progr Oceanogr 106, 49–61. https://doi.org/10.1016/j.pocean.2012.06.006.

Masson, S., Delecluse, P., Boulanger, J.P., Menkes, C., 2002. A model study of the seasonal variability and formation mechanisms of the barrier layer in the eastern equatorial Indian Ocean. J Geophys Res Oceans 107. https://doi.org/10.1029/2001JC000832 (C12):SRF-18.

Masud-Ul-Alam, M., Khan, M.A.I., Barrett, B.S., Rivero-Calle, S., 2022. Surface temperature and salinity in the northern Bay of Bengal: in situ measurements compared with satellite observations and model output. J Appl Rem Sens 16 (1), 018502. https://doi.org/10.1117/1.JRS.16.018502.

Masud-Ul-Alam, M., Khan, A.I., Sunny, S.K., Rahman, A., Rahman, M.S., Mahmud, B., Shaheen, A.R., 2020. An exclusive in-situ dataset on physicochemical parameters in the gappynorthern Bay of Bengal. Data Brief 31, 106024. https://doi.org/10.1016/j.dib.2020.106024.

McPhaden, M.J., Foltz, G.R., Lee, T., Murty, V.S.N., Ravichandran, M., Vecchi, G.A., Vialard, J., Wiggert, J.D., Yu, L., 2009a. Ocean-atmosphere interactions during cyclone nargis. Eos Trans American Geophys Union 90 (7), 53–54. https://doi.org/10.1029/2009EO070001.

McPhaden, M.J., Meyers, G., Ando, K., Masumoto, Y., Murty, V.S.N., Ravichandran, M., Syamsudin, F., Vialard, J., Yu, L., Yu, W., 2009b. Supplement to RAMA: the research moored array for African–Asian–Australian monsoon analysis and prediction. Bull. Am. Meteorol. Soc. 90 (ES5-ES8). https://doi.org/10.1175/2008BAMS2608.2.

Mei, W., Primeau, F., McWilliams, J.C., Pasquero, C., 2013. Sea surface height evidence for long-term warming effects of tropical cyclones on the ocean. PNAS 110 (38), 15207–15210. https://doi.org/10.1073/pnas.1306753110.

Mellor, G.L., Yamada, T., 1982. Development of a turbulence closure model for geophysical fluid problems. Rev. Geophys. 20 (4), 851–875. https://doi.org/10.1029/RG020i004p00851.

Mignot, J., de Boyer, Montégut C., Lazar, A., Cravatte, S., 2007. Control of salinity on the mixed layer depth in the world ocean: 2. Tropical areas. J Geophys Res Oceans 112 (C10). https://doi.org/10.1029/2006JC003953.

Montégut, C.B., Vialard, J., Shenoi, S.S., Shankar, D., Durand, F., Ethé, C., Madec, G., 2007. Simulated seasonal and interannual variability of the mixed layer heat budget in the northern Indian Ocean. J. Climate 20 (13), 3249–3268. https://doi.org/10.1175/JCLI4148.1.

Narvekar, J., Kumar, S.P., 2014. Mixed layer variability and chlorophyll a biomass in the Bay of Bengal. Biogeosciences 11, 3819–3843. https://doi.org/10.5194/bg-11-3819-2014.

Navaneeth, K.N., Martin, M.V., Joseph, K.J., Venkatesan, R., 2019. Contrasting the upper ocean response to two intense cyclones in the Bay of Bengal. Deep Sea Res Part I Oceanogr Res Papers 147, 65–78. https://doi.org/10.1016/j.dsr.2019.03.010.

Nyadjro, E.S., Subrahmanyam, B., Shriver, J.F., 2011. Seasonal variability of salt transport during the Indian Ocean monsoons. J Geophys Res Oceans 116 (C8). https://doi.org/10.1029/2011JC006993.

Obasi, G.O.P., 1997. WMO's programme on tropical cyclone. Mausam 48 (2), 103–112.

Palmen, E., 1948. On the formation and structure of tropical hurricanes. Geophys 3 (1), 26–38.

Pant, V., Girishkumar, M.S., Udaya Bhaskar, T.V.S., Ravichandran, M., Papa, F., Thangaprakash, V.P., 2015. Observed interannual variability of near-surface salinity in the Bay of Bengal. J Geophys Res Oceans 120 (5), 3315–3329. https://doi.org/10.1002/2014JC010340.

Prakash, K.R., Pant, V., 2017. Upper oceanic response to tropical cyclone Phailin in the Bay of Bengal using a coupled atmosphere-ocean model. Ocean Dyn. 67 (1), 51–64. https://doi.org/10.1007/s10236-016-1020-5.

Price, J.F., 1981. Upper Ocean response to a hurricane. J. Phys. Oceanogr. 11 (2), 153–175. https://doi.org/10.1175/1520-0485(1981)011%3C0153:UORTAH%3E2.0.CO;2.

Qiao, F., Wang, G., Khokiattiwong, S., Akhir, M.F., Zhu, W., 2018. Xiao B (2019) China published ocean forecasting system for the 21st-century maritime silk road on December 10. Acta Oceanol Sin 38 (1), 1–3. https://doi.org/10.1007/s13131-019-1365-y.

Qiu, S., Liu, K., Wang, D., Ye, J., Liang, F., 2019. A comprehensive review of ocean wave energy research and development in China. Renew. Sustain. Energy Rev. 113, 109271 https://doi.org/10.1016/j.rser.2019.109271.

Rao, D.V.B., 1987. Numerical simulation of tropical-cyclone circulation using Arakawa-Schubert cumulus parameterization. Il Nuovo Cimento C 10 (6), 677–696. https://doi.org/10.1007/BF02507908.

Rao, R.R., Sivakumar, R., 2003. Seasonal variability of sea surface salinity and salt budget of the mixed layer of the North Indian Ocean. J Geophys Res Oceans 108 (C1), 3009. https://doi.org/10.1029/2001JC000907.

Rao, A.D., Dash, S., Jain, I., Dube, S.K., 2007. Effect of estuarine flow on ocean circulation using a coupled coastal-bay estuarine model: an application to the 1999 Orissa cyclone. Nat. Hazards 41 (3), 549–562. https://doi.org/10.1007/s11069-006-9049-2.

Schade, L.R., 2000. Tropical cyclone intensity and sea surface temperature. J. Atmos. Sci. 57 (18), 3122–3130. https://doi.org/10.1175/1520-0469(2000)057%3C3122:TCIASS%3E2.0.CO;2.

Sengupta, D., Raj, G.N.B., Shenoi, S.S.C., 2006. Surface freshwater from Bay of Bengal runoff and Indonesian throughflow in the tropical Indian Ocean. Geophys. Res. Lett. 33 (22), L22609. https://doi.org/10.1029/2006GL027573.

Sérazin, G., Penduff, T., Grégorio, S., Barnier, B., Molines, J.M., Terray, L., 2015. Intrinsic variability of sea level from global ocean simulations: spatiotemporal scales. J. Climate 28 (10), 4279–4292. https://doi.org/10.1175/JCLI-D-14-00554.1.

Sharma, R., Agarwal, N., Momin, I.M., Basu, S., Agarwal, V.K., 2010. Simulated sea surface salinity variability in the tropical Indian Ocean. J. Climate 23 (24), 6542–6554. https://doi.org/10.1175/2010JCLI3721.1.

Shchepetkin, A.F., McWilliams, J.C., 2005. The regional oceanic modeling system (ROMS): a split-explicit, free-surface, topography-following-coordinate oceanic model. Ocean Model. 9 (4), 347–404. https://doi.org/10.1016/j.ocemod.2004.08.002.

Shee, A., Sil, S., Gangopadhyay, A., Gawarkiewicz, G., Ravichandran, M., 2019. Seasonal evolution of oceanic upper layer processes in the northern Bay of Bengal following a single Argo float. Geophys. Res. Lett. 46 (10), 5369–5377. https://doi.org/10.1029/2019GL082078.

Shenoi, S.S.C., Shankar, D., Shetye, S.R., 2002. Differences in heat budgets of the near-surface Arabian Sea and Bay of Bengal: implications for the summer monsoon. J Geophys Res Oceans 107 (C6), 3052. https://doi.org/10.1029/2000JC000679.

Sil, S., Gangopadhyay, A., Gawarkiewicz, G., Pramanik, S., 2021. Shifting seasonality of cyclones and western boundary current interactions in Bay of Bengal as observed during Amphan and Fani. Sci. Rep. 11 (1), 22052. https://doi.org/10.1038/s41598-021-01607-6.

Somayajulu, Y., Murty, V., Sarma, Y., 2003. Seasonal and inter-annual variability of surface circulation in the Bay of Bengal from TOPEX/Poseidon altimetry. Deep-Sea Res Part II 50, 867–880. https://doi.org/10.1016/S0967-0645(02)00610-0.

Song, Y., Haidvogel, D., 1994. A semi-implicit ocean circulation model using a generalized topography-following coordinate system. J. Comput. Phys. 115 (1), 228–244. https://doi.org/10.1006/jcph.1994.1189.

Sreenivas, P., Gnanaseelan, C., Prasad, K.V.S.R., 2012. Influence of El Niño and Indian Ocean dipole on sea level variability in the Bay of Bengal. Glob Planet Change 80, 215–225. https://doi.org/10.1016/j.gloplacha.2011.11.001.

Stommel, H.M., 1958. The Gulf Stream: A Physical and Dynamical Description. University of California Press, Berkeley, California.

Subrahmanyam, B., Murty, V.S.N., Sharp, R.J., O'Brien, J.J., 2005. Air-sea coupling during the tropical cyclones in the Indian Ocean: a case study using satellite observations. Pure Appl. Geophys. 162 (8), 1643–1672. https://doi.org/10.1007/s00024-005-2687-6.

Sun, J., Wang, D., Hu, X., Ling, Z., Wang, L., 2019. Ongoing poleward migration of tropical cyclone occurrence over the western North Pacific Ocean. Geophys. Res. Lett. 46 (15), 9110–9117. https://doi.org/10.1029/2019GL084260.

Thadathil, P., Muraleedharan, P.M., Rao, R.R., Somayajulu, Y.K., Reddy, G.V., Revichandran, C., 2007. Observed seasonal variability of barrier layer in the Bay of Bengal. J Geophys Res Oceans 112 (C2), C02009. https://doi.org/10.1029/2006JC003651.

Vialard, J., Delecluse, P., 1998. An OGCM study for the TOGA decade. Part I: role of the salinity in the physics of the Western Pacific fresh Pool. J. Phys. Oceanogr. 28, 1071–1088. https://doi.org/10.1175/1520-0485(1998)028<1071: AOSFTT>2.0.CO;2.

Vialard, J., Menkes, C., Boulanger, J.P., Delecluse, P., Guilyardi, E., McPhaden, M.J., Madec, G., 2001. A model study of oceanic mechanisms affecting equatorial Pacific Sea surface temperature during the 1997–98. El Niño 31, 1649–1675. https://doi.org/10.1175/1520-0485(2001)031<1649:AMSOOM>2.0.CO;2.

Vidya, P.J., Das, S., 2017. Contrasting Chl-a responses to the tropical cyclones thane and Phailin in the Bay of Bengal. J. Mar. Syst. 165, 103–114. https://doi.org/10.1016/j.jmarsys.2016.10.001.

Vinayachandran, P.N., Masumoto, Y., Yamagata, T., Mikawa, T., 1999. Intrusion of the southwest monsoon current into the Bay of bengal. J. Geophys. Res. 104 (C5), 11077–11085. https://doi.org/10.1029/1999JC900035.

Vinayachandran, P.N., Murty, V.S.N., Babu, V.R., 2002. Observations of barrier layer formation in the Bay of Bengal during summer monsoon. J Geophys Res Oceans 107. https://doi.org/10.1029/2001JC000831 (C12):SRF-19.

Vinayachandran, P.N., Shankar, D., Vernekar, S., Sandeep, K.K., Amol, P., Neema, C.P., Chatterjee, A., 2013. A summer monsoon pump to keep the Bay of Bengal salty. Geophys. Res. Lett. 40 (9), 1777–1782. https://doi.org/10.1002/grl.50274 Vorosmarty CJ, Fekete BM, Tucker BA (1998) Global River discharge, 1807-1991. Version 1.1 (RivDIS). ORNL DAAC.

Vörösmarty, Charles, J., Fekete, B.M., Tucker, B.A., 1998. Discarge compilation from The Global River Discharge (RivDIS) Project. Distributed Active Archive Center, Oak Ridge National Laboratory, PANGAEA. https://doi.org/10.1594/PANGAEA.859439.

Walker, N.D., Leben, R.R., Balasubramanian, S., 2005. Hurricane-forced upwelling and chlorophyll a enhancement within cold-core cyclones in the Gulf of Mexico. Geophys. Res. Lett. 32 (18) https://doi.org/10.1029/2005GL023716.

Wu, L., Rutgersson, A., Sahlée, E., 2015. Upper-ocean mixing due to surface gravity waves. J Geophys Res Oceans 120 (12), 8210–8228. https://doi.org/10.1002/2015JC011329.

Wyrtki, K., Bennett, E.B., Rochford, D.J., 1971. Oceanographic Atlas of the International Indian Ocean Expedition. National Science Foundation, Washington, DC.

Zheng, Z.W., Ho, C.R., Zheng, Q., Lo, Y.T., Kuo, N.J., Gopalakrishnan, G., 2010. Effects of preexisting cyclonic eddies on upper ocean responses to category 5 typhoons in the western North Pacific. J Geophys Res Oceans 115 (C9). https://doi.org/10.1029/2009JC005562.